

RICE UNIVERSITY

Light Emission in Plasmonic Nanostructures

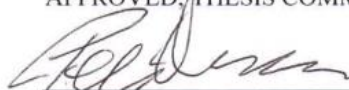
by

Behnaz Ostovar

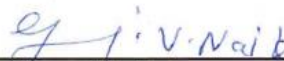
A THESIS SUBMITTED
IN PARTIAL FULFILLMENT OF THE
REQUIREMENTS FOR THE DEGREE

Master of Science

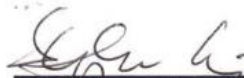
APPROVED, THESIS COMMITTEE



Dr. Peter Nordlander
Professor of Physics and Astronomy and
Electrical and Computer Engineering



Dr. Gururaj Naik
Assistant Professor of Electrical and
computer engineering



Dr. Stephan Link, Chair
Professor of Chemistry and Electrical and
Computer Engineering

HOUSTON, TEXAS
July 2019

Abstract

Light Emission in Plasmonic Nanostructures

by

Behnaz Ostovar

Photoinduced light emission from plasmonic nanoparticles has attracted considerable interest within the scientific community because of its potential applications in novel sensing, imaging, and nanothermometry. One of the suggested mechanisms for the light emission from plasmonic nanoparticles is the radiative recombination of hot carriers through inter- and intraband transitions enhanced by surface plasmons. Here we provide further evidence for this mechanism by precisely determining the effects of size on the light emission from nanoparticles through a systematic survey of gold nanorods (AuNRs) with similar aspect ratios. Using single particle photoluminescence and scattering spectroscopy along with correlated scanning electron microscopy and finite-difference time domain simulations, we calculate the emission quantum yields and Purcell enhancement factors of individual AuNRs. Our results register a strong size dependent quantum yield in AuNRs, resulting in higher quantum yields for smaller AuNRs. Furthermore, separating the contributions of inter- and intraband transitions show an increase in the geometry-assisted intraband transitions in the emission of 20–30 nm wide AuNRs. The calculated 2.3 times stronger electric field confinement in smaller AuNRs provides the necessary momentum mismatch to allow efficient radiative recombination through intraband transitions compared to larger AuNRs with weaker field confinement.

Acknowledgments

I would like to express my appreciation to all the people who made this research possible. First of all, I would like to thank my advisor Professor Stephan Link for all his guidance, support, and encouragement.

I would like to thank Professor Peter Nordlander for his collaboration on this project and his constructive feedback and discussions.

Special thanks to Dr. Lawrence (Joey) Tauzin and Yiyu Cai for their mentorship, training and patience, especially during my first years of grad school. I'd like to thank both of them for their scientific discussions and contributions to this project.

I wish to express my gratitude to all members of the Link and Landes research group for providing a friendly and supportive work environment. Many thanks to my collaborators in Nordlander's group for their collaboration in this work. Also, thanks to all the members of the Laboratory for Nanophotonics (LANP) at Rice University for the great and helpful discussions in the monthly poster sessions. I would also like to thank all my friends in Houston, I am very thankful for all their help, support and encouragement.

And at last but not least, I would like to thank my Family, for being the keystone of my life and their permanent love and support.

~Behnaz

Contents

Abstract.....	ii
Acknowledgments	iii
Contents	iv
List of Figures.....	vi
List of Equations	xiii
Nomenclature	xiv
Introduction.....	1
1.1. Motivation	1
1.2. Overview	2
Background on Metal PL	5
2.1. Metal Film PL	5
2.2. PL of Nanoparticles.....	6
2.2.1. Enhanced Emission Compared to Films.....	6
2.3. Theories on PL Origins	7
Correlated Single Particle Scattering, and Photoluminescence Spectroscopy	9
3.1. Single Particle Dark field Scattering Spectroscopy	9
3.2. Single Particle Photoluminescence Spectroscopy	13
3.3. Polarization Dependence of One Photon PL.....	16
3.4. Power Dependence of One Photon PL.....	18
Exploring Size Dependency of Interband and Intraband Transitions into the Light Emission of Gold Nanorods.....	20
4.1. Introduction	20
4.2. Results and Discussion.....	23
4.2.1. Size Dependent Characterization of Correlated Single Particle Emission and Scattering Spectra	23
4.2.2. Scaled Emission Spectra of AuNRs with Varying Widths.....	35
4.2.3. FDTD Simulations of Electric Field Distributions	38
4.2.4. Scaled Emission Intensities vs Correlated Purcell Enhancement Factors	41

4.3. Conclusion.....	45
4.4. Acknowledgements	45
Methods.....	46
5.1. Sample Preparation and Characterization	46
5.2. Quantum Yield Calculations and PL Spectral Scaling.....	50
5.3. FDTD Simulations	52
5.3.1. FDTD Simulations of AuNRs Absorption Cross Sections.....	52
5.3.2. Near Field Electric Field Distribution Using FDTD Simulations	56
5.3.3. Mode Volume Calculation.....	57
Conclusions and Outlook	59
6.1. Overall Conclusions	59
6.2. Outlook.....	60
References.....	61

List of Figures

Figure 3-1 Schematic illustration of the optical setup for correlated single particle dark field scattering and photoluminescence measurements⁴⁰. For the measurements in the DFS mode the 50/50 beamsplitter, notch filter and long pass filters were taken out. The pinhole in this configuration acts as a spatial filter to remove the excess scattered light. The laser, 50/50 beam splitter, notch filters, and long pass filters were only used on the PL measurements and not in DFS measurements..... 10

Figure 3-2 (A) Dark field scattering image of a 20 μm x 20 μm area including single particle AuNRs (B) The correlated dark field scattering spectrum of the circled AuNR in (A) collected using the confocal geometry described in Figure 3-1..... 12

Figure 3-3 (A) Correlated experimental DFS spectrum and Lorentzian fit of a representative AuNR. Single Lorentzian curve were used to obtain E_{res} and Γ of all DFS spectra of AuNRs. Prior to applying the fitting curve, the measured spectra were converted to an energy scale expressed in eV..... 13

Figure 3-4 (A) Photoluminescence scanning image of a 20 μm x 20 μm area including single particle AuNRs (B) The correlated PL spectrum of the circled AuNR in (A) collected using the confocal geometry described in Figure 3-1..... 15

Figure 3-5 Polarization dependence of the emission spectra of a single AuNR. The emission spectra are obtained with 488 nm excitation as the detection polarization was varied. Inset illustrates the integrated intensity of the area under the spectral region corresponding to all the wavelengths as a function of detected polarization. A \cos^2 curve was fitted to the data points as indicated with the blue dashed line. The excitation light is circularly polarized..... 17

Figure 3-6 (A) Linear dependence of PL spectra on the excitation power indicates one photon PL process. Each data point is acquired by integration of PL spectra over the entire spectral range and then normalized to the maximum data point. Error bars were calculated from at least three PL measurements in a random order. 19

Single particle DFS and PL spectra were recorded for a number of particles from each sample and exhibited broadening of the DFS spectra and evolution of the PL lineshape as the size of the AuNRs increased.^{19-20, 40, 44, 69} Representative DFS and PL spectra of small, medium, and large AuNRs are presented in Figure 4-2 A-C; the details for the characterization of length, width, and aspect ratio distributions of the three samples are presented in chapter 5. Our measurements were performed in the one-photon excitation limit, as demonstrated by the linear dependence of the PL

intensity on the excitation power and a corresponding power law exponent of 1 are demonstrated in Figure 4-6, Figure 4-7, and Figure 4-8, for small, medium and large samples correspondingly.⁴⁴⁻⁴⁶ As the AuNR size increases, the DFS linewidth broadens due to increased radiation damping and, even though the aspect ratios are similar, there is a redshift in the longitudinal LSPR wavelength due to retardation effects (Figure 4-2 A-C).^{11, 44, 70-72} The long wavelength resonance in the PL spectra follows the longitudinal LSPR seen in DFS, but is slightly blueshift, in agreement with previous studies.^{13-15, 37-38, 40, 73-74} The blueshift of the PL emission spectra increases with increasing AuNR size (Figure 4-2 A-C) and is quantified for all AuNRs in Figure 4-1. This resonance has contributions from both inter- and intraband transitions.^{13, 43, 66} 23

Figure 4-2 Representative correlated single particle emission and scattering spectra from small, medium and large AuNRs samples with sizes of (A) 25×61 nm and plasmon resonance wavelength of 612 nm, (B) 49×91 nm with plasmon resonance wavelength of 606 nm, (C) 81×151 nm with its plasmon resonance wavelength located at 651 nm. Corresponding SEM image of each AuNR is shown in the inset of each panel. The scale bar shows 100 nm. All emission spectra are shown in solid lines and dotted lines indicate scatterings spectra. All obtained spectra are normalized to the intensity of their corresponding maximum near their LSPR wavelength as a guide to eye. 25

Figure 4-3 Representative emission polarization dependence of the PL spectra from small AuNRs sample with 488 nm excitation wavelength. Polarization with angle of 0° corresponds to the alignment parallel to the long axis of the AuNR. Inset SEM image corresponds to the correlated AuNR with the width of 25 nm and length of 62 nm. The scale bar shows 100 nm. Red and blue marked spectral regions show the integrated area to investigate on the emission polarization dependency of interband and LSPR spectral regions, respectively. Upper inset demonstrates the polarization dependency of the red color coded region near LSPR wavelength. Dotted black line shows the \cos^2 fit to the integrated intensities near LSPR region of the emission spectra as a function of polarizer's degree. Our results here are in great agreement with previously reported emission polarization dependence.⁷⁹ Lower inset figure demonstrate the lack of polarization dependency of the blue color coded region near the interband peak, in agreement with previous works.⁴⁶ 26

Figure 4-4 Representative emission polarization dependence of the PL spectra from medium AuNRs sample with 488 nm excitation wavelength. Polarization with angle of 0° corresponds to the alignment parallel to the long axis of the AuNR. Inset SEM image corresponds to the correlated AuNR with the width of 47 nm and length of 89 nm. The scale bar shows 100 nm. Red and blue marked spectral regions show the

integrated area to investigate on the emission polarization dependency of interband and LSPR spectral regions, respectively. Upper inset demonstrates the polarization dependency of the red color coded region near LSPR wavelength. Dotted black line shows the Cos^2 fit to the integrated intensities near LSPR region of the emission spectra as a function of polarizer's degree. Our results here are in great agreement with previously reported emission polarization dependence.⁷⁹ Lower inset figure demonstrate the lack of polarization dependency of the blue color coded region near the interband peak, in agreement with previous works.⁴⁶ 27

Figure 4-5 Representative emission polarization dependence of the PL spectra from large AuNRs sample with 488 nm excitation wavelength. Polarization with angle of 0° corresponds to the alignment parallel to the long axis of the AuNR. Inset SEM image corresponds to the correlated AuNR with the width of 80 nm and length of 157 nm. The scale bar shows 100 nm. Red and blue marked spectral regions show the integrated area to investigate on the emission polarization dependency of interband and LSPR spectral regions, respectively. Upper inset demonstrates the polarization dependency of the red color coded region near LSPR wavelength. Dotted black line shows the Cos^2 fit to the integrated intensities near LSPR region of the emission spectra as a function of polarizer's degree. Our results here are in great agreement with previously reported emission polarization dependence.⁷⁹ Lower inset figure demonstrate the lack of polarization dependency of the blue color coded region near the interband peak, in agreement with previous works.⁴⁶ 29

Figure 4-6 (A) The excitation power dependence of the emission spectra for a representative AuNR small sample. Excitation powers used for 488 nm source are indicated in legends. Inset shows the corresponding SEM image of the AuNR with the width of 29 nm and length of 65 nm. The scale bar corresponds to 100 nm. Red and blue marked spectral regions correspond to the integrated area to investigate on the excitation power dependency of interband and LSPR wavelength regions, respectively. (B) Spectrally resolved linear dependence of red-marked spectral region on the excitation power indicates one-photon emission process for this region. Each data point obtained from integration over the red-marked spectral range in panel (A). The error bars of the power-dependent data points were obtained by measuring the emission spectrum at every excitation power three times in random order. (C) Spectrally resolved linear dependence of blue-marked spectral region on the excitation power indicates one-photon emission process for this region. Each data point obtained from integration over the blue-marked spectral range in panel (A). The error bars of the power-dependent data points were obtained by measuring the emission spectra at every excitation power three times in random order. 30

Figure 4-7 (A) The excitation power dependence of the emission spectra for a representative AuNR medium sample. Excitation powers used for 488 nm source are indicated in legends. Inset shows the corresponding SEM image of the AuNR with the width of 46 nm and length of 88 nm. The scale bar corresponds to 100 nm. Red and blue marked spectral regions correspond to the integrated area to investigate on the excitation power dependency of interband and LSPR wavelength regions, respectively. **(B)** Spectrally resolved linear dependence of red-marked spectral region on the excitation power indicates one-photon emission process for this region. Each data point obtained from integration over the red-marked spectral range in panel (A). The error bars of the power-dependent data points were obtained by measuring the emission spectrum at every excitation power three times in random order. **(C)** Spectrally resolved linear dependence of blue-marked spectral region on the excitation power indicates one-photon emission process for this region. Each data point obtained from integration over the blue-marked spectral range in panel (A). The error bars of the power-dependent data points were obtained by measuring the emission spectra at every excitation power three times in random order. 31

Figure 4-8 (A) The excitation power dependence of the emission spectra for a representative AuNR large sample. Excitation powers used for 488 nm source are indicated in legends. Inset shows the corresponding SEM image of the AuNR with the width of 88 nm and length of 153 nm. The scale bar corresponds to 100 nm. Red and blue marked spectral regions correspond to the integrated area to investigate on the excitation power dependency of interband and LSPR wavelength regions, respectively. **(B)** Spectrally resolved linear dependence of red-marked spectral region on the excitation power indicates one-photon emission process for this region. Each data point obtained from integration over the red-marked spectral range in panel (A). The error bars of the power-dependent data points were obtained by measuring the emission spectrum at every excitation power three times in random order. **(C)** Spectrally resolved linear dependence of blue-marked spectral region on the excitation power indicates one-photon emission process for this region. Each data point obtained from integration over the blue-marked spectral range in panel (A). The error bars of the power-dependent data points were obtained by measuring the emission spectra at every excitation power three times in random order. 32

Figure 4-9 Cumulative distributions for the blueshift of the wavelength of maximum of emission spectra near their LSPR wavelength from that of scattering spectra in three samples color coded. The blueshift is increasing as the size of AuNRs gets larger in agreement with previous reports.⁴⁰ The average blueshift for the small, medium and large AuNRs samples are 10.14 nm, 22.19 nm and 36.47 nm, respectively. 34

Figure 4-10 (A) Scaled emission spectra of five different sizes of AuNRs using their correlated QY. Excitation wavelength of 488 nm was used to measure the emission spectra. Correlated SEM image of AuNRs shown in the legend are color coded with their corresponding emission spectrum. Obtained sizes of AuNRs are 27×61 nm, 30×67 nm, 40×90 nm, 50×104 nm, and 84×150 nm. The scale bar shows 100 nm. Inset: Integrated intensity of grey marked area for all 120 AuNRs registering a slight size dependency for the interband peak of different sizes. The minor decrease in intensity can origin from the residuals of the tails of the main peak into the interband peak. **(B)** PDOS simulations of the correlated AuNRs as **(A)** using FEM (Comsol Multiphysics 5.4). The simulated PDOS profile agrees well with the experimental emission spectra in the obtained spectral lineshape and emission maximum near their plasmon resonance wavelength. However, the proportional maximum intensity of different sizes near their plasmon resonance wavelength deviates between simulated PDOS profiles and experimental emission spectra..... 37

Figure 4-11 FDTD simulation of $|E|^2$ distribution in the near field at the substrate-AuNR interface. Schematic illustration of simulated AuNRs with sizes of **(A)** 27×66 nm and **(B)** 85×149 nm representing the small and large samples, respectively. $|E|^2$ distributions at the substrate-AuNR interface plane for **(C)** 27×66 nm and **(D)** 85×149 nm AuNR. White dashed lines are used to draw the line sections in **(E)** and **(F)**. Line section of the electric field along the y-axis of AuNRs to estimate the d for **(C)** 27×66 nm and **(D)** 85×149 nm AuNR. The estimated d represents the distance over which the electric field varies. 40

Figure 4-12 Maximum intensity of scaled emission spectra of AuNRs near their surface plasmon resonance wavelengths as a function of their correlated Q-factors. Q-factors of individual AuNRs are obtained from their single particle scattering spectra by dividing their surface plasmon energy to their spectral linewidth. Data points are color coded for small (green), medium (orange) and large (purple) samples of AuNRs. Gray line is a linear fit to the data points of AuNRs from large sample demonstrating an expected enhancement as the size gets smaller based on Purcell enhancement factor. Q-factor of individual AuNRs has a linear relationship with their Purcell enhancement factor (PDOS) as reported previously⁴⁰. The linear fit expected assuming that contribution of interband and intraband transitions to the emission spectra of AuNRs remains constant between different sizes and only their Purcell enhancement factor increases. Deviation of data points from expected enhancement (gray line) has been attributed to the increased contribution of intraband transitions in smaller sizes. Error bars on data points have been obtained with binning steps of 5 for Q-factors. 43

Figure 4-13 Mode volume (blue line and open circles) and physical volume (open squares) as a function of AuNR width. Solid green circles show the quality factor (Q-Factor) of the same individual AuNRs obtained from their respective DFS spectra as described in the main text. All calculations are in agreement with a previous study.⁹⁰ Mode volumes are calculated for 23 AuNRs chosen using random sampling without replacement. The mode volume is different than the physical volume for these AuNRs. Smaller AuNRs have mode volumes comparable to their physical volume, but as the size increases and the mode volume differs from the physical volume, because the electric field is mainly confined near the metal surface. 44

Figure 5-1 Characterization of small AuNR sample (29 x 63 nm). (A) Representative scheme of small AuNR sample (B) Histograms of aspect ratio, (C) width, and (D) length obtained from SEM images of all measured AuNRs in the small samples. ... 47

Figure 5-2 Characterization of medium AuNR sample (45 x 87 nm). (A) Representative scheme of medium AuNR sample (B) Histograms of aspect ratio, (C) width, and (D) length obtained from SEM images of all measured AuNRs in the medium samples. 48

Figure 5-3 Characterization of large AuNR sample (77 x 153 nm). (A) Representative scheme of large AuNR sample (B) Histograms of aspect ratio, (C) width, and (D) length obtained from SEM images of all measured AuNRs in the large samples. ... 49

Figure 5-4 The configuration of AuNRs used in FDTD simulations (Lumerical). An AuNR approximated by a capped hemispherical cylinder and its 3.5 nm CTAB shell layer accounting for the ligand molecules is indicated by a white arrow that sits on the quartz substrate. The quartz substrate and air medium are also marked in the figure. The circularly polarized excitation source is depicted by the magenta arrow that excited the AuNR from top. The circularly polarized light is used to mimic the un-polarized illumination used in the experiment. The refractive index of quartz was set to 1.52 and that of CTAB shell was chosen to be 1.44⁹⁵. The dielectric constants of bulk gold was employed from experimental results of Johnson and Christy⁹⁶. The PML were used to surround the entire system. 54

Figure 5-5 Correlated FDTD scattering cross section and experimental DFS spectrum agree well. (A) SEM image of the AuNR with the width of 30.4 nm and length of 67.7 nm. (B) Schematic representative of the simulated AuNR in FDTD. Best match with experimental scattering maximum was obtained by varying the width and length within 1 nm. Simulated AuNR with size of 30 nm x 68 nm provided the best match. (C) Correlated experimental DFS of AuNR presented in (A) with its FDTD simulated counterpart in (B). Maximum of experimental DFS and simulated scattering cross section were 618 nm and 619 nm, respectively. 55

Figure 5-6 FDTD simulation of the absorption cross section of a single AuNR with sizes of 30 nm x 68 nm. The maximum of absorption cross section occurs around 615 nm suggesting a strong relationship to the LSPR of simulated AuNR. The calculated absorption cross section at 488 nm for individual AuNRs is used in their QY calculations. 55

Figure 5-7 Schematic illustration of the used geometries to find the near field electric field distribution of the AuNRs at the particle-substrate interface plane. 57

List of Equations

Equation 4.1 – Definition of Purcell Factor.....	41
Equation 4.2 – Defenition of Q-Factor.....	41
Equation 5.1 – Definition of QY	50
Equation 5.2 – Number of emitted photons.....	50
Equation 5.3 – Number of absorbed photons.....	51
Equation 5.4 – Scaling PL spectrum	51
Equation 5.5 – Mode volume calculation.....	57

Nomenclature

SERS	Surface-Enhanced Raman Spectroscopy
LSPR	Localized Surface Plasmon Resonance
AuNRs	Gold Nanorods
FDTD	Finite Difference Time Domain
PL	Photoluminescence
QY	Quantum Yield
DFS	Dark Field Scattering
APD	Avalanche Photodiode
CCD	Charge-Coupled Device
Q-Factors	Quality Factors
cw	Continuous Wave
TEM	Transmission Electron Microscopy
SEM	Scanning Electron Microscopy
PDOS	Photonic Density of States
FEM	Finite Element Method
CTAB	Cetyltrimethylammonium Bromide

Chapter 1

Introduction

1.1. Motivation

Light emission from plasmonic noble metal nanostructures have potential applications in novel imaging,¹⁻³ sensing,⁴⁻⁷ and nanothermometry.⁸⁻⁹ Also, Surface-enhanced Raman spectroscopy (SERS) shows the presence of the light emission as a continuum background.¹⁰ Therefore, understanding the emission mechanism is critical to improve the aforementioned applications.

The surface plasmon resonance of metallic nanoparticles, defined as the collective oscillation of conduction band electrons, governs most of their optical properties.¹¹ Light emission from plasmonic nanoparticles demonstrates strong dependence on the surface plasmon and the geometry of the particle.¹² While it is well accepted that the localized surface plasmon

resonance (LSPR) can enhance the emission,¹³⁻¹⁷ and there are lots of studies on the effects of LSPR on the emission,^{13, 18-20} there is a great need to study the geometry effect on light emission.²¹ Ultimately, characterizing the optical properties of the plasmonic nanoparticles will help to maximize the efficiency of associated applications.

1.2. Overview

Chapter 2 gives insight about the background of the light emission from metals. It first describes the emission from smooth metal film and its low quantum yield of 10^{-10} . The emission is enhanced for films with a roughened surface due to their ability to host surface plasmons. Light emission from single-particles is then discussed and the critical role of the surface plasmon as an enhancing factor is described. In the last part of this chapter, developed theories on the origin of emission from metallic nanoparticles are discussed.

Chapter 3 describes the single-particle measurement optical setup used for simultaneous scattering and photoluminescence spectroscopy of gold nanorods (AuNRs). A representative correlated scattering and photoluminescence measurements of a gold nanorod is presented. The AuNR scattering spectrum is characterized to quantify the surface plasmon resonance energy and spectral linewidth. Moreover, emission polarization and power dependence behavior of an individual AuNR is studied and the expected behavior discussed.

The text and figures in the sections 3.1 and 3.2 of this chapter were adapted from a manuscript titled, “Breaking momentum conservation in smaller gold nanorods enhances light emission” by Behnaz Ostovar, Yi-Yu Cai, Lawrence J. Tauzin, Stephen A. Lee, Arash Ahmadvand, Runmin

Zhang, Nathan Diemle, Patrick J. Straney, Jill E. Millstone, Peter Nordlander, and Stephan Link.

This manuscript is ready to be submitted.

Chapter 4 aims to explore the size dependent light emission of AuNRs of similar aspect ratios and variable widths. Similar aspect ratios are chosen so that the AuNRs have similar plasmon resonances. We found that quantum yield of AuNRs show a size dependency behavior and increases as the size shrinks. Furthermore, we quantified the contribution of inter- and intraband transitions on quantum yield for different sizes. We also confirmed the effect of electric field confinement in allowing the momentum forbidden intraband transitions into the light emission. Our size dependent study can be used in optimizing light harvesting applications such as imaging, sensing, and nanothermometry.

The text and figures in of this chapter were adapted from a manuscript titled “Breaking momentum conservation in smaller gold nanorods enhances light emission” by Behnaz Ostovar, Yi-Yu Cai, Lawrence J. Tauzin, Stephen A. Lee, Arash Ahmadvand, Runmin Zhang, Nathan Diemle, Patrick J. Straney, Jill E. Millstone, Peter Nordlander, and Stephan Link. This manuscript is ready to be submitted.

Chapter 5 includes the experimental and theoretical methods used in the experimental sections of this thesis. Details on Finite Difference Time Domain (FDTD) simulations of absorption cross sections and electric field distributions is also discussed. The calculation methods used in this thesis to find the quantum yield of single gold nanorods from their correlated photoluminescence measurements and absorption cross sections are explained. The size distribution of three samples of gold nanorods used in the chapter 4 has been also characterized.

The text and figures in this chapter were adapted from a manuscript titled “Breaking momentum conservation in smaller gold nanorods enhances light emission” by Behnaz Ostovar, Yi-Yu Cai, Lawrence J. Tauzin, Stephen A. Lee, Arash Ahmadvand, Runmin Zhang, Nathan Diemle, Patrick J. Straney, Jill E. Millstone, Peter Nordlander, and Stephan Link. This manuscript is ready to be submitted.

Chapter 6 contains the concluding remarks of the thesis, and also provides a perspective on the future directions of the research on the emission of metallic nanoparticles.

Chapter 2

Background on Metal PL

2.1. Metal Film PL

Photoluminescence (PL) of gold films was first reported in 1969 by Mooradian.²² They observed a broadband unpolarized luminescence spectrum from gold film upon excitation with a 488 nm argon laser. PL from bulk gold was attributed to the emission of photon after the radiative recombination of electron–holes that have been excited from d-band to the sp-conduction band near the L symmetry in the Brillouin zone of the bulk gold. This electron–hole interband recombination is an inefficient process with a low quantum yield (QY) of 10^{-10} .

Later on Boyd et al. studied PL from roughened gold films and showed several order of magnitude enhancement in the PL of rough surfaces compared to that of smooth films.²³ The observed enhancement was attributed to the contribution of momentum forbidden intraband transitions.²³⁻²⁴ Enhanced electric fields at LSPR of rough edges resulted in improvement of both excitation and emission efficiency. Highly confined electric fields relaxed symmetry and momentum conservation rules allowing intraband transitions.²⁴⁻²⁶ Critical role of LSPR in plasmonic structures have been described as an antenna projecting the light emission to the far-field.²⁷

2.2. PL of Nanoparticles

2.2.1. Enhanced Emission Compared to Films

Since this first observation PL enhancements due to localized surface plasmons, this matter has been subject of many studies. The effects of LSPR on enhancing the PL of nanoparticles has been first conducted on nanoparticles of different sizes and shapes in solutions. By studying gold nanospheres with 5 nm diameter Wilcoxon et al. reported QY of $\sim 10^{-5}$ to 10^{-4} for their ensemble measurements.²⁶ AuNRs of different aspect ratios ranging from 2.4 to 5.4 was studied by Mohammed et al. where they reported 10^{-4} – 10^{-3} QYs for their ensemble measurements.²⁷ Gold nanospheres with diameters of 2 to 60 nm

were reported to have a QY of $\sim 10^{-6}$ independent of size by Dulkeith et al.²⁸ These ensemble studies report an enhanced PL from gold nanoparticles compared to that of gold film but their QYs have 2-3 orders of magnitude difference. These variations can be attributed to the inhomogeneity of the measured sample.

By conducting single particle measurements Gaiduk et al. reported a size independent QY with average of $\sim 3 \times 10^{-7}$ on gold nanospheres with sizes of 5 to 80 nm.²⁹ Single particle studies on AuNRs showed a QY in order of $\sim 8 \times 10^{-6}$ and the central role of LSPR was investigated.¹⁵ AuNRs with different aspect ratios have been studied to investigate on the effect of LSPR wavelength on the QY and a decrease in QY is reported when LSPR of the AuNRs were moving from excitation wavelength.^{19-21, 30}

2.3. Theories on PL Origins

Despite the enormous studies on the PL of gold nanoparticles its exact mechanism is not yet very well understood. However, important role of LSPR in the PL of plasmonic gold nanoparticles have been discussed due to enhancement of QY from 10^{-10} to 10^{-6} and resembling the dark field scattering (DFS) spectrum.¹⁴⁻¹⁵ Initial mechanism trying to explain the origin of this resemblance by stating that the PL is the direct radiative of

plasmon relaxation itself.²⁷ Then it was argued that hot carriers generated through either inter- or intra-band excitation are responsible for the observed emission.^{24, 27, 31-34} The created hot carriers enhanced through plasmonic modes act as the main PL channels for enhancing the emission through an antenna effect.²⁷ There is also another research suggesting that emission from metal nanoparticles might be a result of electronic Raman scattering mechanism.^{10, 35-36} Despite the difference in the proposed origins of the emission, all studies acknowledge the role of plasmon resonance as an enhancing antenna in light emission.^{14, 27-28, 37-39}

Chapter 3

Correlated Single Particle Scattering, and Photoluminescence Spectroscopy

3.1. Single Particle Dark field Scattering Spectroscopy

A home-built single particle setup based on an inverted Zeiss microscope (Zeiss Axio Observer.D1m) was used for all the single particle measurements of this work.⁴⁰ Schematic representation of the optical setup is illustrated in **Figure 3-1**.

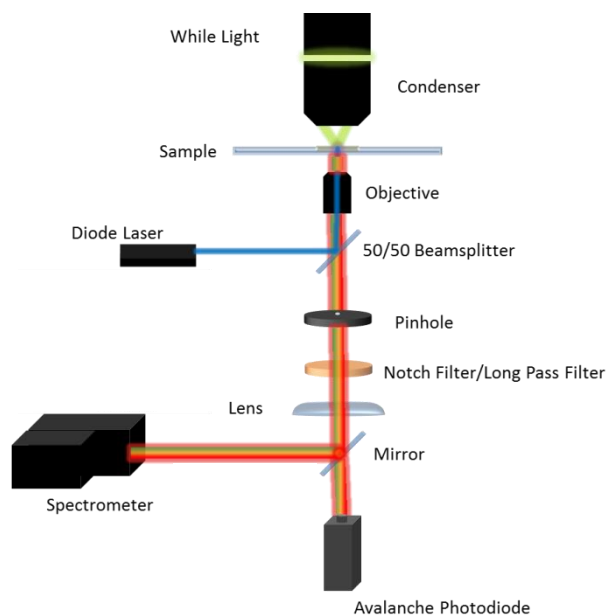


Figure 3-1 Schematic illustration of the optical setup for correlated single particle dark field scattering and photoluminescence measurements⁴⁰. For the measurements in the DFS mode the 50/50 beamsplitter, notch filter and long pass filters were taken out. The pinhole in this configuration acts as a spatial filter to remove the excess scattered light. The laser, 50/50 beam splitter, notch filters, and long pass filters were only used on the PL measurements and not in DFS measurements.

In our correlated configuration, DFS measurements were conducted first. A wide field image recorded on a digital single-lens reflex camera was collected and the same image was later used to locate the particles in the DFS and PL spectroscopy measurements. A halogen lamp (Zeiss HAL 100) was used as an excitation source focused on the sample

using an oil immersion dark field condenser. A 50x objective with a 0.8 numerical aperture (Zeiss EC Epiplan-Neofluar) was used to collect the scattered light. The light was passed through a pinhole with a 50 μm diameter (Thorlabs P50S) to achieve a confocal geometry by spatially filtering the light. A DFS image was constructed by moving the sample with a piezo scanning stage (Physik Instrumente P-517.3CL) and detecting the spatially filtered light on an avalanche photodiode (APD, PerkinElmer SPCM-AQRH-15). Single particle DFS spectra of the imaged particles were obtained by redirecting the signal of each particle to a spectrometer (Shamrock SR193i-A) connected to a charge-coupled device (CCD) camera (Andor iDus 420 BEX2-DD). The spectra recorded with an integration time of 3 seconds were background subtracted with signal from an area near the nanoparticle where no other nanoparticles were located. The spectra were corrected for the white light spectrum by dividing by the white light spectrum from the halogen lamp obtained by switching to the transmitted light mode of the condenser and recording the spectrum with the same CCD camera. An example of a raster DFS scanned image of an area of AuNRs is shown in **Figure 3-2A**. The DFS spectra of the marked particle in **Figure 3-2A** with a blue circle is shown in **Figure 3-2B**. The homogeneous linewidth (Γ) and resonance energy (E_{res}) of measured DFS spectra were determined from a Lorentzian fit as shown in **Figure 3-3**. Prior to the Lorentzian fitting, the measured spectra were converted to an energy scale expressed in eV then analyzed for fitting. The resonance energy and linewidth obtained from Lorentzian fitting of single particle DFS measurements were then used to calculate the quality factor (Q-Factor) for individual AuNRs using **Error! Reference source not found.****Error! Reference source not found..**

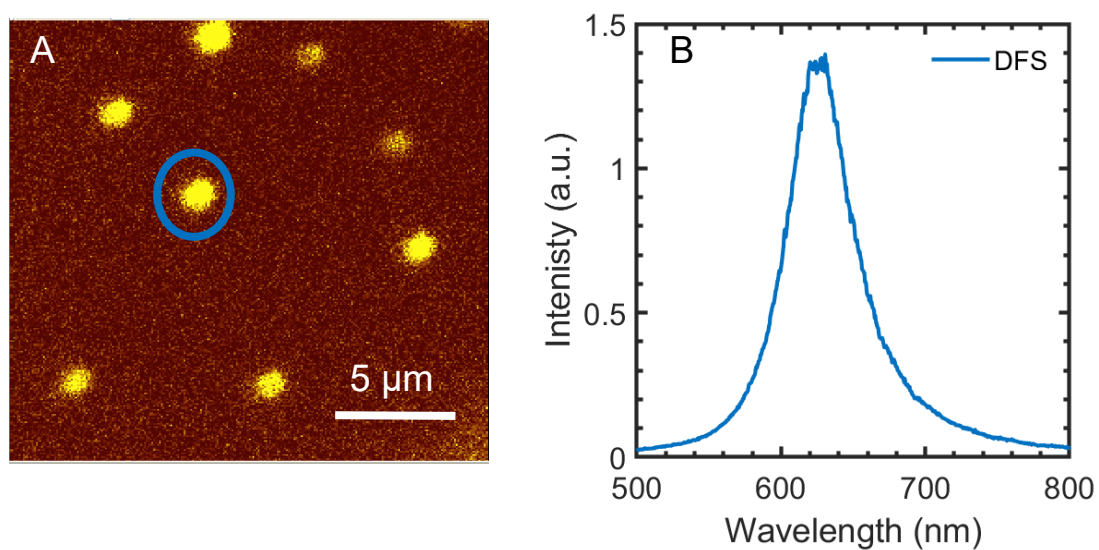


Figure 3-2 (A) Dark field scattering image of a 20 μm x 20 μm area including single particle AuNRs (B) The correlated dark field scattering spectrum of the circled AuNR in (A) collected using the confocal geometry described in Figure 3-1.

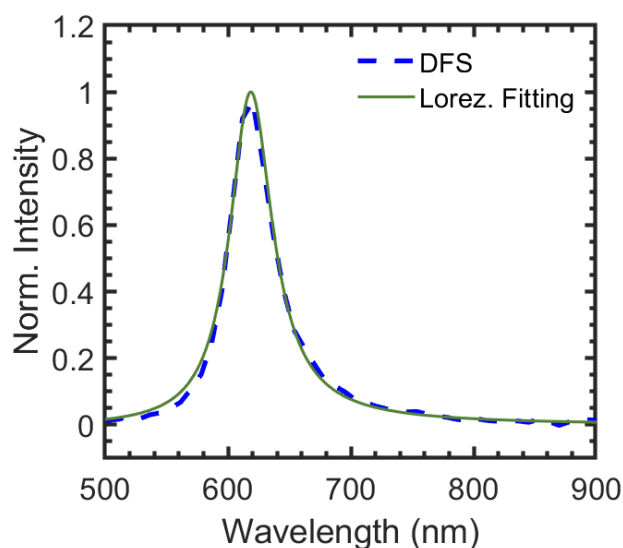


Figure 3-3 (A) Correlated experimental DFS spectrum and Lorentzian fit of a representative AuNR. Single Lorentzian curve were used to obtain E_{res} and Γ of all DFS spectra of AuNRs. Prior to applying the fitting curve, the measured spectra were converted to an energy scale expressed in eV.

3.2. Single Particle Photoluminescence Spectroscopy

Correlated confocal emission images and spectra were collected immediately after measuring the corresponding DFS using the same instrument (**Figure 3-1**). For emission spectroscopy, in **Figure 3-1**, a 488 nm continuous wave diode laser (Coherent OBIS) was used as the excitation source and was directed to the sample with a 50/50

dichroic mirror (Chroma). The pinhole was removed from the detection path and a 488 nm notch filter (Semrock) together with a 496 nm long pass filter (Semrock) were used to reject the excitation source and transmit the emission. A depolarizer (Edmund Optics Quartz Lyot Depolarizer) was used before the spectrometer to remove any polarization bias. For each nanoparticle three emission spectra with a 20 second exposure time were collected and averaged. The background signal for each nanoparticle was then measured on a blank area near the nanoparticle. The emission spectra were analyzed after background subtraction and adjustment for detection efficiency. The detection efficiency of the setup for different wavelengths was corrected by using a calibrated lamp (Ocean Optics LS-1 Cal) as described previously.³⁹ The laser powers were measured after the objective at the sample plane for each measurement. The laser beam size had a full width at half-maximum of 394 nm as obtained from AuNR images. The excitation power density was limited to $1.1 \times 10^5 \text{ W/cm}^2$ to prevent damaging the nanoparticles. Larger excitation power densities were used in the power dependence measurements, but we always checked for nanoparticle damage by recording a second DFS spectrum after the emission measurements and only considered nanoparticles that showed no changes. The emission image and spectra of the region as **Figure 3-2** are shown in **Figure 3-4**.

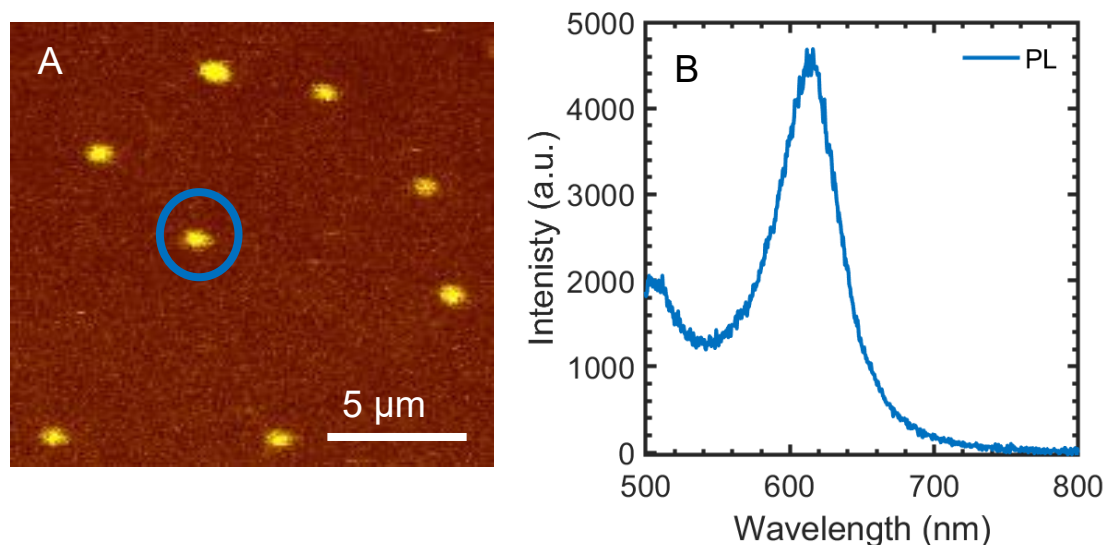


Figure 3-4 (A) Photoluminescence scanning image of a 20 μm x 20 μm area including single particle AuNRs (B) The correlated PL spectrum of the circled AuNR in (A) collected using the confocal geometry described in Figure 3-1.

In order to achieve the correlated DFS and PL spectroscopy indexed quartz slides (AdValue Tech) were used. Indexed Au film pattern was achieved by evaporating Au on carbonless copper Transmission Electron Microscopy (TEM) grids with indexed patterns (Ted Pella) that were then peeled off from the substrate, resulting in on gold patterns on the clean quartz. In our correlated configuration, DFS measurements were conducted first. An image using a Single-Lens Reflex camera was first carried out for spatial correlation purpose in the dark field configuration and the same image was later used to locate the particles in DFS and PL spectroscopy measurements.

3.3. Polarization Dependence of One Photon PL

Polarization dependence study has been conducted to further demonstrate the role of LSPR in the PL mechanism from AuNRs. It has been shown that the plasmon resonance of a particle has a perfect dipole response showing a strong polarization dependence.⁴¹ Therefore if the PL is related to the LSPR it ought to demonstrate the same polarization dependence.^{14, 42-43} The polarization dependence investigations on the PL of single AuNRs have demonstrated a strong dependence of PL properties on the excitation and emission polarization.^{14, 44} Emission polarization dependence of PL spectra of an AuNR with the excitation wavelength of 488 nm has been conducted by inserting a polarizer in the collection path. The PL spectra shown in **Figure 3-5** are acquired by rotating the polarizer's angle. The polarization dependence behavior is shown in the inset of **Figure 3-5** by analyzing the integrated intensity of the area under the spectral region corresponding to all the wavelengths. A trigonometric function is used to fit data as shown in blue dashed line in the inset of **Figure 3-5**. The strong polarization dependence of PL spectra demonstrates that the emission is linked to the LSPR of individual AuNRs in agreement with previous studies.^{40, 43} Polarization dependence of PL of AuNRs with different sizes have been discussed in detail in Chapter 4.

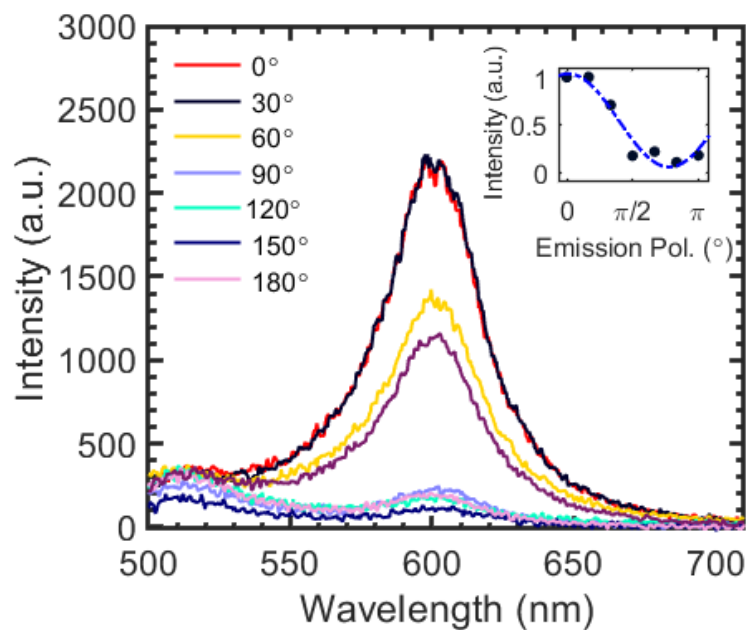


Figure 3-5 Polarization dependence of the emission spectra of a single AuNR. The emission spectra are obtained with 488 nm excitation as the detection polarization was varied. Inset illustrates the integrated intensity of the area under the spectral region corresponding to all the wavelengths as a function of detected polarization. A \cos^2 curve was fitted to the data points as indicated with the blue dashed line. The excitation light is circularly polarized.

3.4. Power Dependence of One Photon PL

The power dependence measurements have been shown as an important factor in finding the underlying recombination processes in the PL studies.⁴⁵ Dependence of the PL intensity of single AuNRs on their excitation power was conducted in this work to investigate their one photon PL process. **Figure 3-6** demonstrates that PL intensity is linearly dependent on the power of excitation source indicating a one photon absorption and emission process, in strong agreement with previous works.^{44, 46} PL intensities are obtained by integrating the PL spectra over the entire spectral region. In order to exclude the chance of melting or reshaping of AuNRs in high powers, DFS of AuNRs is acquired before and after PL measurements.

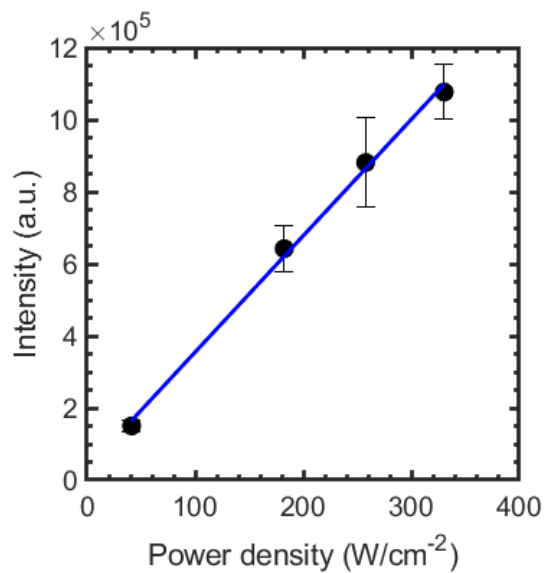


Figure 3-6 (A) Linear dependence of PL spectra on the excitation power indicates one photon PL process. Each data point is acquired by integration of PL spectra over the entire spectral range and then normalized to the maximum data point. Error bars were calculated from at least three PL measurements in a random order.

Chapter 4

Exploring Size Dependency of Interband and Intraband Transitions into the Light Emission of Gold Nanorods

4.1. Introduction

Plasmonic nanoparticles have attracted the attention of researchers in recent years because of their broad range of applications in novel sensing,⁴⁻⁶ imaging,¹⁻² nanothermometry,^{8, 47-48} photocatalysis,^{7, 49-50} and photocurrent generation.⁵¹⁻⁵² To date, several studies have demonstrated the importance of hot carrier generation and distribution as a function of plasmonic nanoparticle geometry,⁵³⁻⁵⁴ such as the nanoparticle size.⁵⁴⁻⁵⁵ Furthermore, the role of inter- and intraband decay processes in the hot carrier distribution has been studied.⁵⁶⁻⁵⁷ Specifically, while efficient hot hole generation through interband transitions has been predicted for gold nanoslabs thicker than 40 nm, confining the geometry increased the probability of generation of hot electrons via intraband transitions.⁵⁷ Enhanced intraband transitions in nanoconfined metal structures is due to the breaking of momentum conservation rules because of the strong electric field confinement caused by localized surface plasmon resonances

(LSPRs).²⁴ Distinct properties of hot electrons and holes have led to different applications for these charge carriers; high energy hot electrons have been reported to be sufficient for bond dissociation reactions,⁵⁸⁻⁶⁰ and hot holes can induce oxidation.⁶¹⁻⁶³ Therefore, further understanding the effect of size on the distribution of hot electrons and holes would enable the rational design of efficient hot carrier based devices.^{53, 56-57, 64}

Due to the complexity of directly probing hot carriers, indirect methods for characterizing their properties have attracted attention.^{13, 65} The emission from plasmonic nanoparticles, ascribed to the radiative recombination of hot electrons and holes generated through inter- and intraband transitions or photoluminescence (PL), presents a unique method for indirect characterization of hot carriers.^{13, 24, 40} Using PL as a probe however requires a proper understating of the mechanism and the relative contributions of inter- and intraband transitions. Emission of metal films was attributed to PL originating from interband transitions between the d-band and the sp-band near the L symmetry point of the Brillouin zone for bulk gold.²² Momentum forbidden intraband transitions were reported to contribute to the PL as well if the surfaces were rough and hence supported LSPRs.²³⁻²⁴ Studies of single AuNRs with well defined plasmon modes also showed radiative recombination of hot carriers via inter- or intraband transitions,^{24, 27, 31-34} which is enhanced by plasmonic modes as quantitatively described with a Purcell effect enhancement mechanism.^{13, 66} An alternative proposed mechanism argues that emission from metal nanoparticles is the result of electronic Raman scattering.^{10, 35-36} A thorough study on the size dependence of inter- and intraband transitions contribution to the emission is necessary to help further differentiate between these two mechanisms.

In this work, we investigate the PL of AuNRs with different widths but similar aspect ratios to determine the size dependence of inter- and intraband transitions. Maintaining a constant aspect ratio is important because changing the aspect ratio tunes the overlap of the LSPR and interband transitions, leading to increased plasmon damping when spectral overlap is larger.⁶⁷ AuNRs of different sizes but similar aspect ratios have been used to study size effects on surface enhanced Raman scattering⁶⁸ and chemical interface damping,⁶⁷ but only a limited number of AuNRs with similar aspect ratios have been investigated and were found to show a slight increase in PL intensity with decreasing size.³⁸ In addition, the reason for the observed intensity increase has remained unclear.³⁸ We use three samples containing small ($29 \pm 2 \times 63 \pm 3$), medium ($45 \pm 5 \times 87 \pm 7$), and large ($77 \pm 9 \times 153 \pm 9$) AuNRs with aspect ratios of ~ 2 . By combining dark field scattering (DFS), PL spectroscopy, and correlated scanning electron microscopy (SEM) we obtain a detailed single particle understanding of the size dependent PL in AuNRs. Experimental results are supplemented with simulations of absorption cross sections based on the correlated SEM images. With the absorption cross sections we calculate emission quantum yields (QYs) of individual AuNRs to directly compare absolute PL intensities among different sizes. We find a size dependent decrease of the PL QY with increasing AuNR size, in agreement with the emission mechanism based on Purcell effect enhanced radiative recombination of hot carriers. Only a weak size dependence is seen for the interband component in the PL spectrum of AuNRs. Our results, supported by finite difference time domain (FDTD) simulations of surface electric fields, furthermore demonstrate that intraband transitions are enhanced in smaller AuNRs due to the relaxation of momentum conservation rules.

4.2. Results and Discussion

4.2.1. Size Dependent Characterization of Correlated Single Particle Emission and Scattering Spectra

Single particle DFS and PL spectra were recorded for a number of particles from each sample and exhibited broadening of the DFS spectra and evolution of the PL lineshape as the size of the AuNRs increased.^{19-20, 40, 44, 69} Representative DFS and PL spectra of small, medium, and large AuNRs are presented in **Figure 4-2** A-C; the details for the characterization of length, width, and aspect ratio distributions of the three samples are presented in chapter 5. Our measurements were performed in the one-photon excitation limit, as demonstrated by the linear dependence of the PL intensity on the excitation power and a corresponding power law exponent of 1 are demonstrated in **Figure 4-6**, **Figure 4-7**, and **Figure 4-8**, for small, medium and large samples correspondingly.⁴⁴⁻⁴⁶ As the AuNR size increases, the DFS linewidth broadens due to increased radiation damping and, even though the aspect ratios are similar, there is a redshift in the longitudinal LSPR wavelength due to retardation effects (**Figure 4-2** A-C).^{11, 44, 70-72} The long wavelength resonance in the PL spectra follows the longitudinal LSPR seen in DFS, but is slightly blueshift, in agreement with previous studies.^{13-15, 37-38, 40, 73-74} The blueshift of the PL emission spectra increases with increasing AuNR size (**Figure 4-2** A-C) and is

quantified for all AuNRs in **Figure 4-1**. This resonance has contributions from both inter- and intraband transitions.^{13, 43, 66}

The short wavelength feature in the PL spectra of the AuNRs, attributed to interband transitions,^{15, 27, 46} varies significantly relative to the long wavelength resonance. Consistent with the assignment of interband transitions and a weak transverse plasmon mode with a reduced quality factor, the short wavelength emission is unpolarized,^{2, 13, 38, 40, 46, 74} in contrast to the strong dipolar emission polarization dependence observed for the long wavelength resonance (It has been illustrated in **Figure 4-3**, **Figure 4-4**, and **Figure 4-5** for small, medium and large sizes, respectively).^{38, 43, 75} The relative ratio between the emission intensities of these two peaks reverses as the AuNRs size increases. The dominant resonance in the emission spectra of small AuNRs is found close to the longitudinal LSPR (**Figure 4-2 A**), while for the large AuNRs interband transitions dominate (**Figure 4-2 C**). Note however that all spectra in **Figure 4-2** are arbitrarily normalized at the longitudinal LSPR to allow for a comparison between DFS and PL spectral features. As the PL intensity scales with the absorption cross section at the excitation wavelength of 488 nm and hence roughly with the volume of the AuNRs,⁷⁶⁻⁷⁸ the intensities as measured cannot be quantitatively compared. However, by calculating the QYs of all individual AuNRs we are able to scale the PL spectra for quantitative assessment between different sizes among all samples.

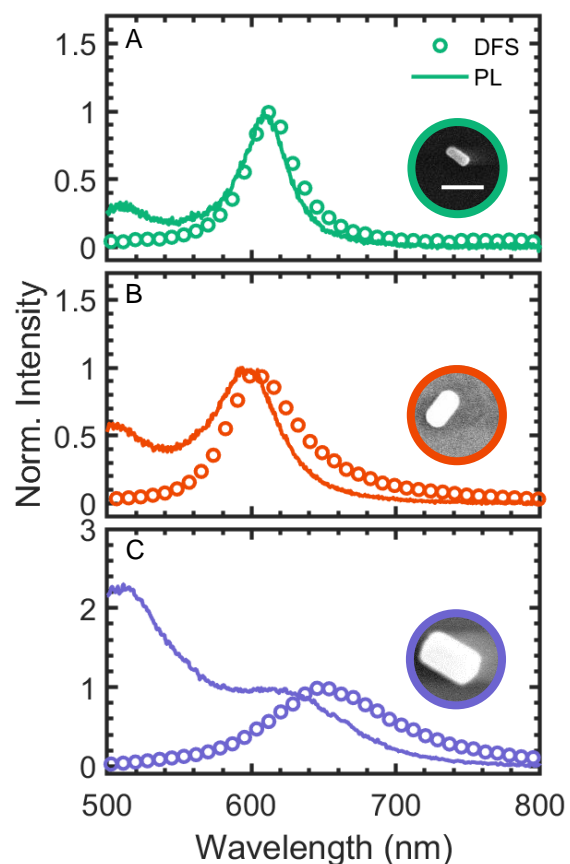


Figure 4-2 Representative correlated single particle emission (line) and scattering (circles) spectra from small, medium, and large AuNR samples with sizes of (A) 25×61 nm and LSPR wavelength of 612 nm, (B) 49×91 nm with LSPR wavelength of 606 nm, and (C) 81×151 nm with its LSPR resonance wavelength located at 651 nm. The corresponding SEM image of each AuNR is shown in the inset of each panel. The spectra are intensity normalized at their corresponding LSPR maximum as a guide to the eye for illustrating spectral differences.

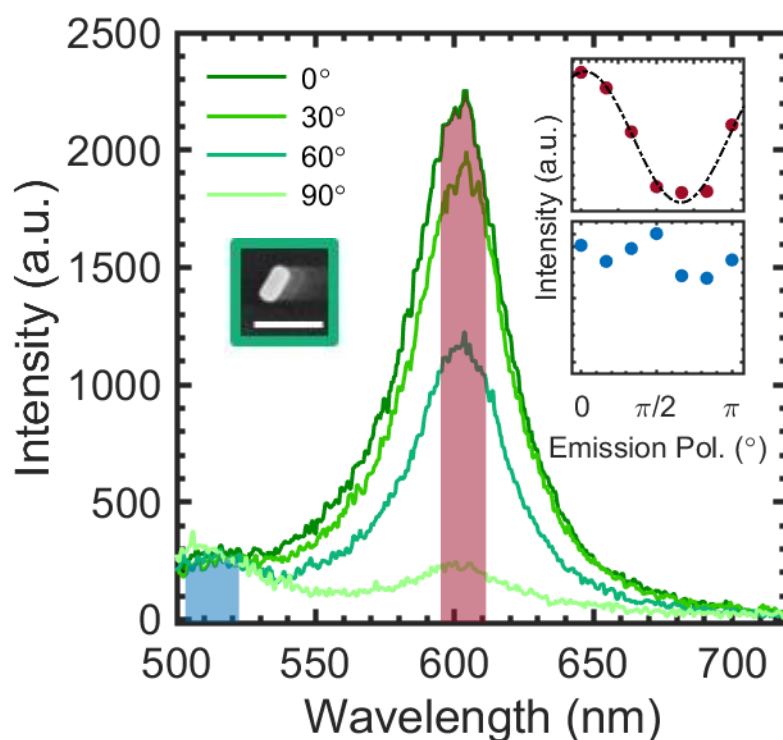


Figure 4-3 Representative emission polarization dependence of the PL spectra from small AuNRs sample with 488 nm excitation wavelength. Polarization with angle of 0° corresponds to the alignment parallel to the long axis of the AuNR. Inset SEM image corresponds to the correlated AuNR with the width of 25 nm and length of 62 nm. The scale bar shows 100 nm. Red and blue marked spectral regions show the integrated area to investigate on the emission polarization dependency of interband and LSPR spectral regions, respectively. Upper inset demonstrates the polarization dependency of the red color coded region near LSPR wavelength. Dotted black line shows the Cos^2 fit to the integrated intensities near LSPR region

of the emission spectra as a function of polarizer's degree. Our results here are in great agreement with previously reported emission polarization dependence.⁷⁹ Lower inset figure demonstrate the lack of polarization dependency of the blue color coded region near the interband peak, in agreement with previous works.⁴⁶

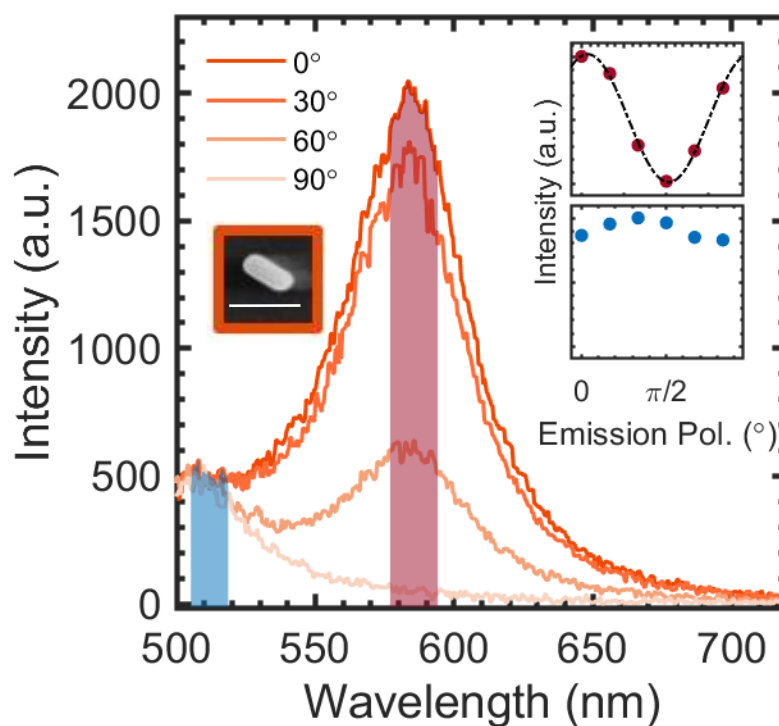


Figure 4-4 Representative emission polarization dependence of the PL spectra from medium AuNRs sample with 488 nm excitation wavelength. Polarization with angle of 0° corresponds to the alignment parallel to the long axis of the AuNR. Inset SEM image corresponds to the correlated AuNR with the width

of 47 nm and length of 89 nm. The scale bar shows 100 nm. Red and blue marked spectral regions show the integrated area to investigate on the emission polarization dependency of interband and LSPR spectral regions, respectively. Upper inset demonstrates the polarization dependency of the red color coded region near LSPR wavelength. Dotted black line shows the Cos^2 fit to the integrated intensities near LSPR region of the emission spectra as a function of polarizer's degree. Our results here are in great agreement with previously reported emission polarization dependence.⁷⁹ Lower inset figure demonstrate the lack of polarization dependency of the blue color coded region near the interband peak, in agreement with previous works.⁴⁶

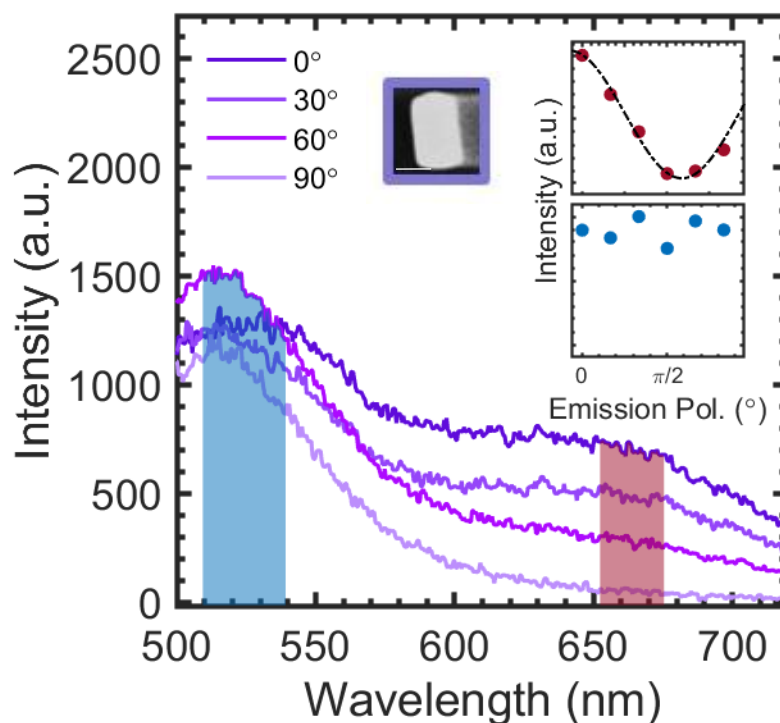


Figure 4-5 Representative emission polarization dependence of the PL spectra from large AuNRs sample with 488 nm excitation wavelength. Polarization with angle of 0° corresponds to the alignment parallel to the long axis of the AuNR. Inset SEM image corresponds to the correlated AuNR with the width of 80 nm and length of 157 nm. The scale bar shows 100 nm. Red and blue marked spectral regions show the integrated area to investigate on the emission polarization dependency of interband and LSPR spectral regions, respectively. Upper inset demonstrates the polarization dependency of the red color coded region near LSPR wavelength. Dotted black line shows the Cos^2 fit to the integrated intensities near LSPR region of the emission spectra as a function of polarizer's degree. Our results here are in great agreement with previously reported emission polarization dependence.⁷⁹ Lower inset figure demonstrate the lack of polarization dependency of the blue color coded region near the interband peak, in agreement with previous works.⁴⁶

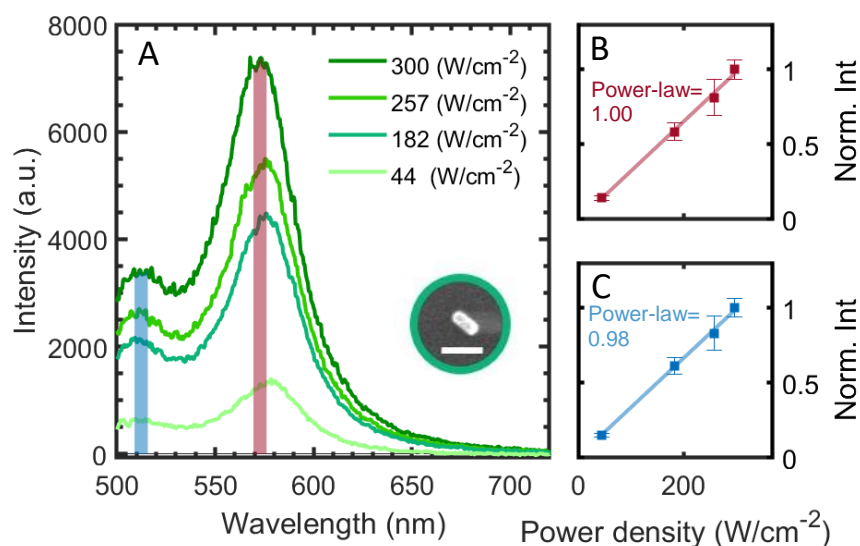


Figure 4-6 (A) The excitation power dependence of the emission spectra for a representative AuNR small sample. Excitation powers used for 488 nm source are indicated in legends. Inset shows the corresponding SEM image of the AuNR with the width of 29 nm and length of 65 nm. The scale bar corresponds to 100 nm. Red and blue marked spectral regions correspond to the integrated area to investigate on the excitation power dependency of interband and LSPR wavelength regions, respectively. **(B)** Spectrally resolved linear dependence of red-marked spectral region on the excitation power indicates one-photon emission process for this region. Each data point obtained from integration over the red-marked spectral range in panel (A). The error bars of the power-dependent data points were obtained by measuring the emission spectrum at every excitation power three times in random order. **(C)** Spectrally resolved linear dependence of blue-marked spectral region on the excitation power indicates one-photon emission process for this region. Each data point obtained from integration over the blue-marked spectral range in panel

(A). The error bars of the power-dependent data points were obtained by measuring the emission spectra at every excitation power three times in random order.

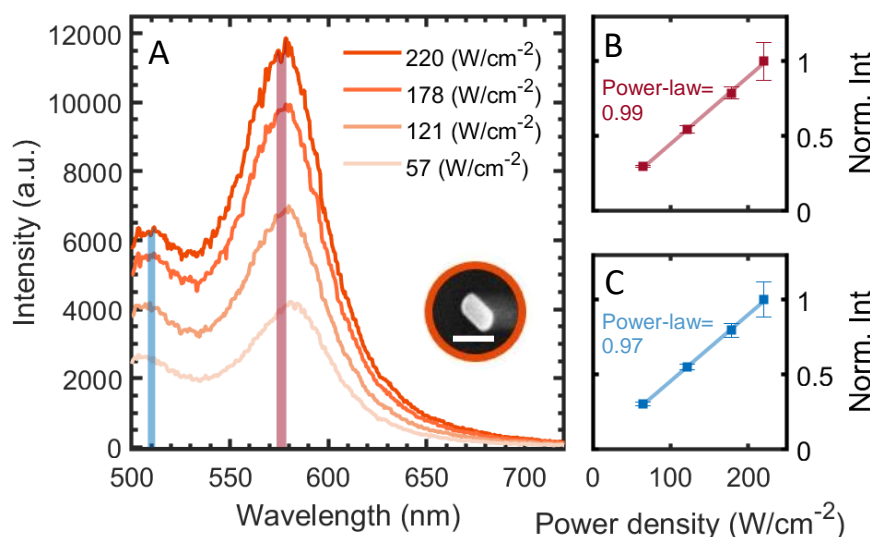


Figure 4-7 (A) The excitation power dependence of the emission spectra for a representative AuNR medium sample. Excitation powers used for 488 nm source are indicated in legends. Inset shows the corresponding SEM image of the AuNR with the width of 46 nm and length of 88 nm. The scale bar corresponds to 100 nm. Red and blue marked spectral regions correspond to the integrated area to investigate on the excitation power dependency of interband and LSPR wavelength regions, respectively. **(B)** Spectrally resolved linear dependence of red-marked spectral region on the excitation power indicates one-photon emission process for this region. Each data point obtained from integration over the red-marked spectral

range in panel (A). The error bars of the power-dependent data points were obtained by measuring the emission spectrum at every excitation power three times in random order. (C) Spectrally resolved linear dependence of blue-marked spectral region on the excitation power indicates one-photon emission process for this region. Each data point obtained from integration over the blue-marked spectral range in panel (A). The error bars of the power-dependent data points were obtained by measuring the emission spectra at every excitation power three times in random order.

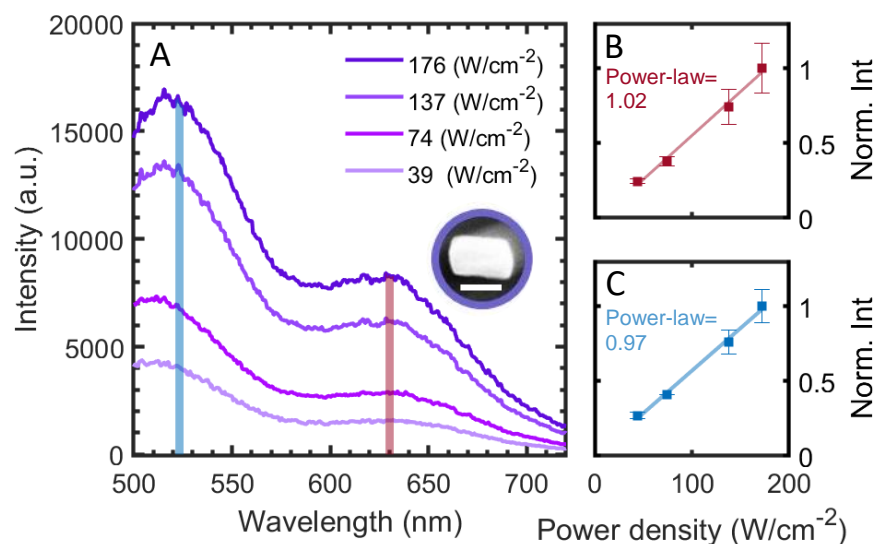


Figure 4-8 (A) The excitation power dependence of the emission spectra for a representative AuNR large sample. Excitation powers used for 488 nm source are indicated in legends. Inset shows the corresponding SEM image of the AuNR with

the width of 88 nm and length of 153 nm. The scale bar corresponds to 100 nm. Red and blue marked spectral regions correspond to the integrated area to investigate on the excitation power dependency of interband and LSPR wavelength regions, respectively. (B) Spectrally resolved linear dependence of red-marked spectral region on the excitation power indicates one-photon emission process for this region. Each data point obtained from integration over the red-marked spectral range in panel (A). The error bars of the power-dependent data points were obtained by measuring the emission spectrum at every excitation power three times in random order. (C) Spectrally resolved linear dependence of blue-marked spectral region on the excitation power indicates one-photon emission process for this region. Each data point obtained from integration over the blue-marked spectral range in panel (A). The error bars of the power-dependent data points were obtained by measuring the emission spectra at every excitation power three times in random order.

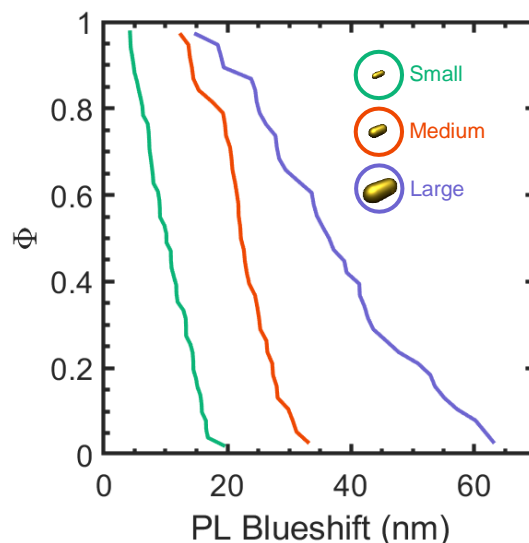


Figure 4-9 Complementary cumulative distributions of the emission maximum shift at the longitudinal surface plasmon resonance (LSPR) from the dark field scattering (DFS) maximum for the small (green), medium (red), and large (purple) AuNRs. Φ illustrates the fraction of nanorods with a value higher than the one indicated on the x-axis. An increasing blueshift is observed as the size of AuNRs becomes larger in agreement with previous reports.⁴⁰ The average blueshift for the small, medium, and large AuNRs are 10.1 nm, 22.1 nm, and 36.5 nm, respectively.

4.2.2. Scaled Emission Spectra of AuNRs with Varying Widths

In contrast to what is suggested by the normalized spectra in **Figure 4-2**, once corrected by individual AuNR QYs a pronounced decrease in the intensity of the long wavelength emission peak is observed as the size increases, while the emission intensity for the interband region is mostly independent of size. **Figure 4-10A** shows emission spectra that are scaled by the respective QY of the 5 different exemplary AuNRs chosen to cover the entire range of sizes. Clearly, the emission resonance close to the longitudinal LSPR drastically decreases in intensity with increasing AuNR size. Fermi's Golden rule states that emission is proportional to the photonic density of states (PDOS) and transition matrix elements connecting the initial and final states.¹³ For larger particle sizes the LSPR is broadened due to increased radiation damping, resulting in a decrease of the Purcell factor, which is proportional to the PDOS, thus causing a decrease in enhanced emission.^{40, 80} On the other hand, the interband peaks in the emission spectra of AuNRs do not show a pronounced size dependence. The inset in **Figure 4-10A** shows the integrated emission for the area marked by the gray bar corresponding to the interband peak for all AuNRs as a function of their width. Interband transitions are intrinsic properties of gold, and thus do not have a size dependence when accounting for particle volume as done here.^{29, 40, 46} The slight decrease in intensity observed with increasing size is likely the result of the tail of the long wavelength resonance overlapping more with the interband emission for the small AuNRs (**Figure 4-2**).

The calculated PDOS of AuNRs with different sizes follows a similar trend to that of the experimental AuNR emission spectra (**Figure 4-10B**). The wavelength dependent PDOS were determined by integrating the radiative PDOS calculated near the boundary

of the AuNRs using the finite element method (Comsol Multiphysics 5.4).^{13, 81} As Figure 2B demonstrates, PDOS spectra capture the LSPR near 600 nm, comparable to the experimental emission spectra. However, comparing the relative intensities of emission spectra in **Figure 4-10A** to the PDOS intensities in **Figure 4-10B**, we find that the experimental emission spectra decrease more strongly with increasing size, suggesting that changes to the transition matrix elements must also occur, in addition to just the PDOS. Although an excess emission intensity decrease in ensemble measurements^{20, 82} or for particles larger than $\sim 1.5 \mu\text{m}$ ⁸³ has been attributed to the re-absorption of emission, this phenomenon has been reported to be negligible in other single particle emission measurements of AuNRs with similar sizes.³⁸

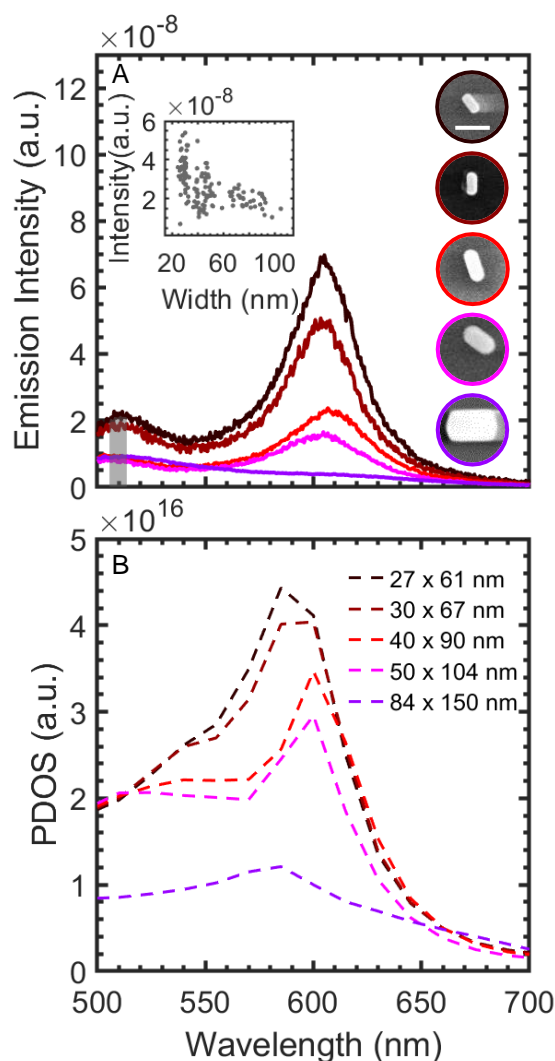


Figure 4-10 (A) (A) Emission spectra of five AuNRs with different sizes scaled based on their QYs. SEM images of the corresponding AuNRs are given on the right. The sizes were 27×61 nm, 30×67 nm, 40×90 nm, 50×104 nm, and 84×150 nm. Inset: Integrated intensity of the area marked by the gray bar (main figure, centered at 509 ± 4 nm), corresponding to the region where interband transitions dominate, for 120 AuNRs with different sizes. (B) PDOS simulations carried out for AuNRs with the same sizes.

4.2.3. FDTD Simulations of Electric Field Distributions

The electric field confinement in plasmonic nanoparticles can assist in breaking the symmetry and momentum conservation rules for intraband transitions.^{24, 34, 68, 84-87} FDTD simulations of a small and large AuNR were performed to obtain the electric field intensity distribution around the AuNRs and to estimate the electric field confinement (**Figure 4-10**). The electric field distributions calculated at the interface between the AuNR and the substrate in the XY plane (**Figure 4-10A,B**) and are more confined for the small AuNR (**Figure 4-10C,E**) compared to those of the large AuNR (**Figure 4-10D,F**), in agreement with previous work.¹² The k vector of confined electric field in the AuNRs can be decomposed into its perpendicular and parallel to the metal surface components, k_{\perp} and k_{\parallel} which can be written as: $k = \sqrt{k_{\parallel}^2 + k_{\perp}^2}$. In confined nanostructures $|k_{\perp}|, |k_{\parallel}| \gg k$.²⁴ The largest wave number present in the near field has been described using $k_{\parallel} \approx \pi/d$, where d corresponds to the distance over which the electric field varies.^{24, 88} Based on our calculations, approximate values of d are 7.7 nm for the small AuNR (**Figure 4-10E**) and 17.9 nm for the large AuNR (**Figure 4-10F**). The effective generation of intraband transitions has been reported for electric fields with $d \approx 5$ nm, similar to the $d = 7.7$ for the small AuNR obtained here.²⁴ The derived k_{\parallel} for the small AuNR is approximately $40 \times 10^7 \text{ cm}^{-1}$ and $10 \times 10^7 \text{ cm}^{-1}$ for the large AuNR. Using the parabolic approximation for the conduction band dispersion and the approximate value of 10^8 cm^{-1} for the Fermi wave number in gold,²⁴ the momentum needed for exciting an electron in the sp-band to energy levels corresponding to the longitudinal LSPR of

AuNRs with aspect ratio of 2 (i.e., 1.96 eV above the Fermi level) is $\Delta k \approx 7 \times 10^7 \text{ cm}^{-1}$. When the rough estimate of Δk needed for intraband transitions and k_{\parallel} provided by the near field electric field distribution are of the same magnitude, direct excitation of electrons within the conduction band is possible.²⁴ Comparing Δk and k_{\parallel} of the two AuNRs demonstrate that the emission spectra of the small AuNRs have a larger contribution from intraband transitions compared to the large AuNRs. It has also been reported that other factors such as phonon coupling, the Umklapp process, and Landau damping can give rise to larger values of k_{\parallel} in small nanoparticles, further supporting the conclusion that the increased PL intensity in smaller nanoparticles arises from an increase of intraband emission transitions that become allowed due to symmetry breaking.⁸⁴

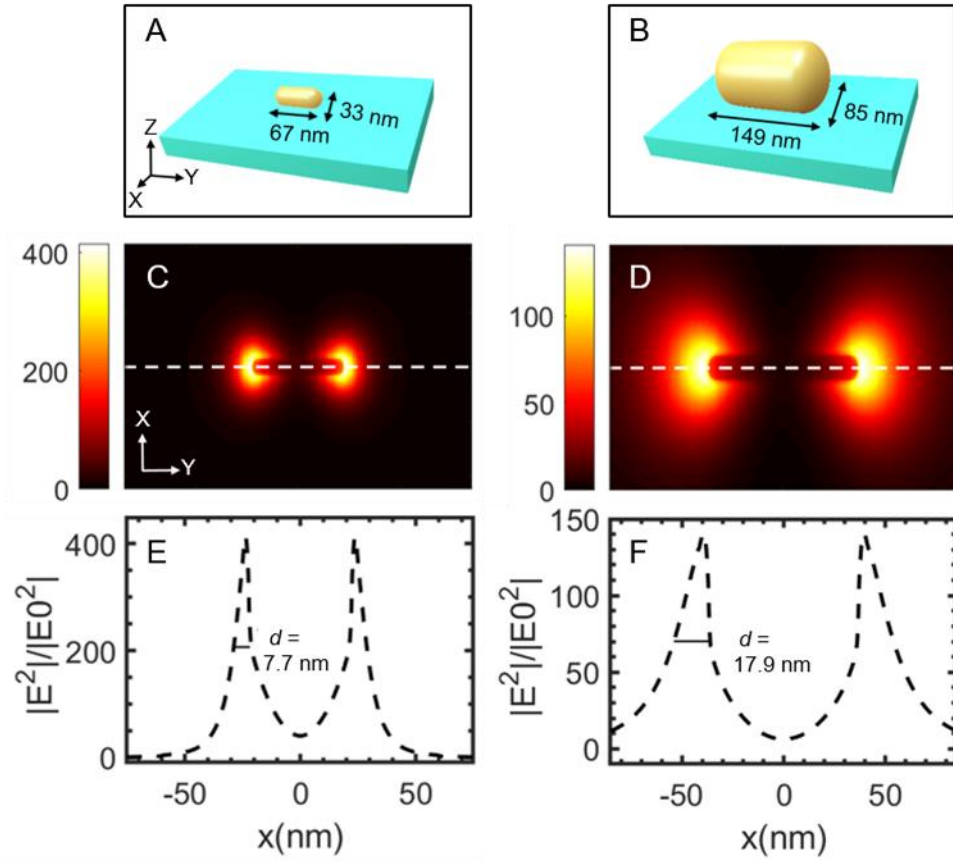


Figure 4-11 FDTD simulations of the $|E|^2/|E_0|^2$ distribution in the near field at the substrate-AuNR interface calculated at the resonance energy. Schematic illustration of the simulated AuNRs with sizes of (A) 33×67 nm and (B) 85×149 nm representing the small and large AuNR samples, respectively. $|E|^2/|E_0|^2$ distributions at the substrate-AuNR interface plane for the (C) 33×67 nm and the (D) 85×149 nm AuNR. White dashed lines indicate the line sections in (E) and (F) taken along the long AuNR axis (y-axis). The confinement of $|E|^2/|E_0|^2$ is estimated by the distance d over which the electric field varies, where d is taken as the full width of the line section at half maximum.

4.2.4. Scaled Emission Intensities vs Correlated Purcell Enhancement Factors

Further quantifying the different contributions of inter- and intraband transitions to the emission spectra of AuNRs confirms that the size dependent PL arises from changes in the contribution from intraband transitions. Based on the Purcell effect PL mechanism, emission enhancement is proportional to the simulated PDOS. Instead of simulating the PDOS, the Purcell factor can also be derived experimentally using the following definition: ⁸⁹⁻⁹⁰

$$Purcell\ factor = \frac{3Q}{4\pi^2 V} \left(\frac{\lambda}{n}\right)^3$$

Equation 4.1 – Definition of Purcell Factor

Here the *Q-Factor* is the quality factor of the cavity resonance (i.e., the AuNR), *V* describes the mode volume, λ is the emission wavelength, and *n* is the refractive index of the surrounding medium and was set to 1.52. The *Q-Factor* is determined from the DFS spectra according to: ^{34, 91}

$$Q = \frac{E_{res}}{\Gamma}$$

Equation 4.2 – Defenition of Q-Factor

Here E_{res} is the resonance energy and Γ is the homogeneous linewidth of the longitudinal LSPR both obtained through fitting to a Lorentzian function.^{34, 91} The mode volumes were calculated using following the approach proposed by Koenderink using **Equation 5.5**.^{90, 92} The measured *Q-Factors* and calculated mode volumes of the AuNRs are presented in **Figure 4-13**. With these values we calculated the Purcell factors for different AuNR sizes using **Equation 4.3**. **Figure 4-12** illustrates the resulting QY scaled emission intensities at the LSPR wavelength as a function of the relative Purcell factor for all 127 AuNRs investigated.

Considering that in large AuNRs the efficient generation of intraband transitions is not possible due to momentum conservation rules,²⁴ we assume that their emission spectra over the entire spectra range is due to mostly interband transitions, which are furthermore size independent. A linear interpolation of the emission intensity at the longitudinal LSPR of large AuNRs versus their Purcell factors predicts the enhancement based only on the PDOS and ignores any changes to the transition matrix elements, as shown by the gray line in **Figure 4-12**. This predicted trend is clearly not followed by the small and medium AuNRs. We attribute the deviation to intraband emission transitions, which increases with decreasing AuNR size. For medium AuNRs (**Figure 4-12**, orange symbols) approximately 55% of the overall emission comes from intraband transitions; in the small AuNRs (**Figure 4-12**, purple symbols) the intraband transition contribution increases to 65%. These values are lower limits because we have assumed that no intraband transitions

occur in the large AuNRs. The observed size dependent increase in intraband contribution to the PL is consistent with the larger $k_{||}$ value calculated for the smaller AuNR. These results indicate that based on Fermi's Golden rule the transition matrix elements change as a function of size, which we attribute to the breaking of and momentum conservation rules for interband transitions.

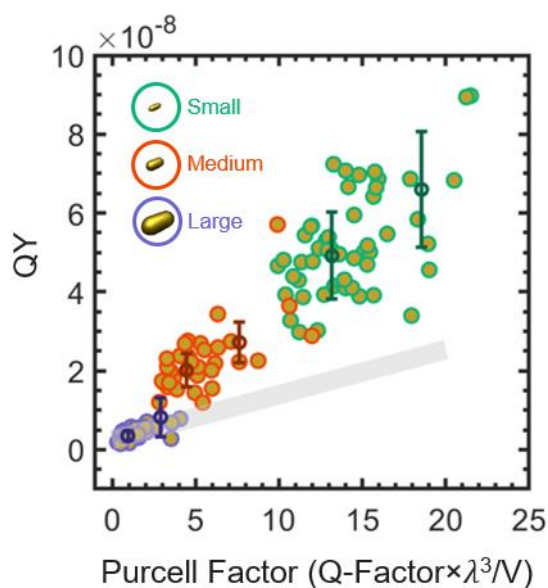


Figure 4-12 QY of AuNRs at their LSPR maximum wavelengths ± 0.5 nm as a function of relative Purcell factor. Data points are color coded for small (green), medium (orange), and large (purple) AuNR samples. The gray line is a linear fit to the data points of AuNRs from the large sample demonstrating the expected enhancement with decreasing size based on the Purcell factor alone. The fit assumes that the emission intensity only scales with Purcell enhancement factor. Error bars correspond to the average and standard deviation from AuNRs with widths that fall in a 15 nm bins.

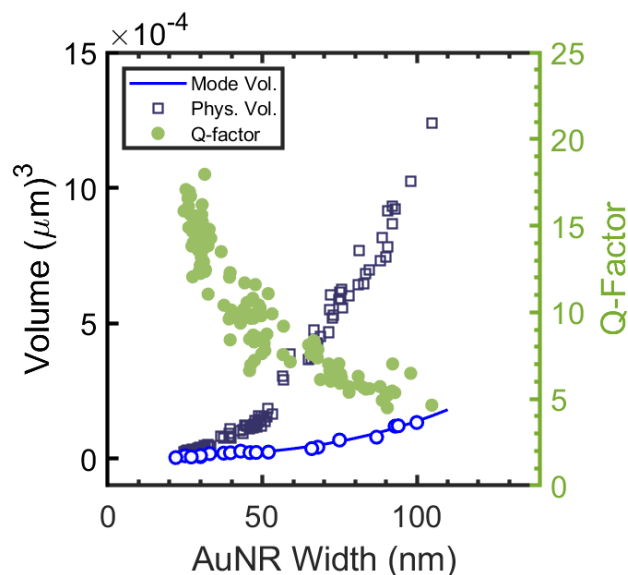


Figure 4-13 Mode volume (blue line and open circles) and physical volume (open squares) as a function of AuNR width. Solid green circles show the quality factor (Q-Factor) of the same individual AuNRs obtained from their respective DFS spectra as described in the main text. All calculations are in agreement with a previous study.⁹⁰ Mode volumes are calculated for 23 AuNRs chosen using random sampling without replacement. The mode volume is different than the physical volume for these AuNRs. Smaller AuNRs have mode volumes comparable to their physical volume, but as the size increases and the mode volume differs from the physical volume, because the electric field is mainly confined near the metal surface.

4.3. Conclusion

We have shown that contribution of intraband transitions into the emission of the AuNRs depends on the size. Our results suggest that in small AuNRs intraband transitions are allowed due to the breaking of symmetry and momentum conservation rules. While interband transitions are the dominant contribution in the emission of large AuNRs. Interband transitions are almost independent from size. Increasing the size of the AuNRs decreases the emission efficiency as expected based on Purcell enhancement mechanism. Our result in agreement with the Fermi's Golden rule demonstrates the role of Purcell enhancement factor in the emission enhancement from AuNRs.

4.4. Acknowledgements

We acknowledge support from the Robert A. Welch Foundation (C-1222 to P.N., C-1664 to S.L.) and the Air Force Office of Scientific Research (MURI FA9550-15-1-0022).

Chapter 5

Methods

5.1. Sample Preparation and Characterization

Chemically synthesized AuNRs were selected from three samples with different sizes, but similar aspect ratios of ~ 2 . The average sizes of the AuNRs in the three samples were $29 \pm 2 \times 63 \pm 3$ nm, $45 \pm 5 \times 87 \pm 7$ nm, and $77 \pm 9 \times 153 \pm 9$; referred to as small, medium, and large respectively. Small and medium AuNRs were synthesized using a modified seed-mediated growth process developed by the Murray group.⁹³ The large AuNRs were synthesized based on a synthesis method by Ming *et al.*⁹⁴ Details of the two synthesis protocols are described in a previous publication.¹³ More details on the size distribution of three samples have been described in **Figure 5-1**, **Figure 5-2** and **Figure 5-3**.

Indexed quartz slides were used as substrates because quartz has a reduced background in emission measurements and thus results in increased signal to noise ratios. A dilute base piranha solution (1:4:20 $\text{NH}_4\text{OH}/\text{H}_2\text{O}_2/\text{H}_2\text{O}$) was used to clean the quartz slides (AdValue Tech). The slides were rinsed twice with Millipore (DI) water and N_2 gas was used to dry the quartz substrates prior to gold evaporation for indexing. An indexed grid was patterned onto the quartz slides by evaporating 35 nm of gold through a TEM grid

shadow mask (Ted Pella), enabling correlated single particle measurements. The indexed quartz slides were then O₂ plasma-cleaned for 2 minutes. An appropriate concentration of AuNRs was spin-coated on the indexed quartz slides for 60s at 2500 rpm for adequate single particle coverage.

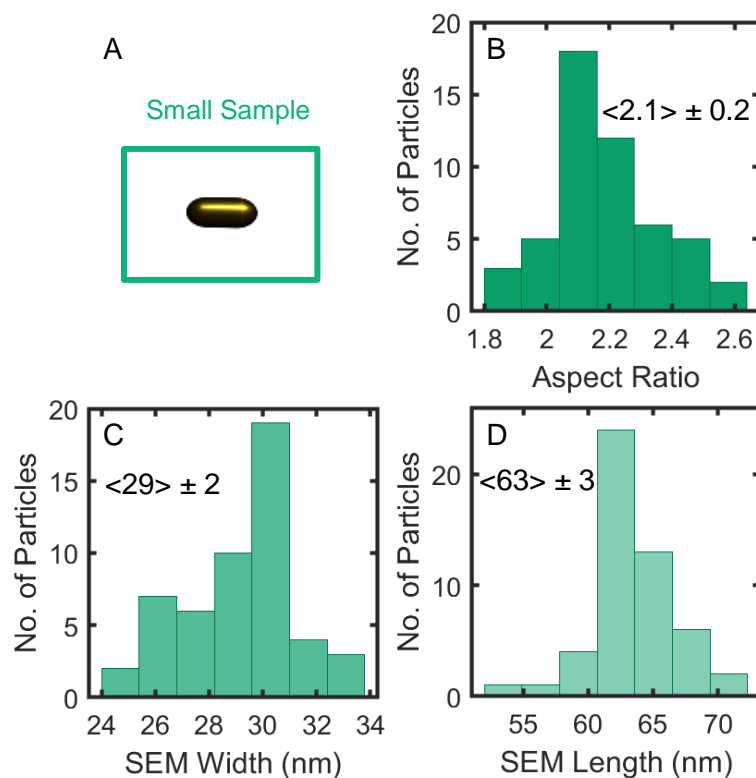


Figure 5-1 Characterization of small AuNR sample (29 x 63 nm). (A) Representative scheme of small AuNR sample (B) Histograms of aspect ratio, (C) width, and (D) length obtained from SEM images of all measured AuNRs in the small samples.

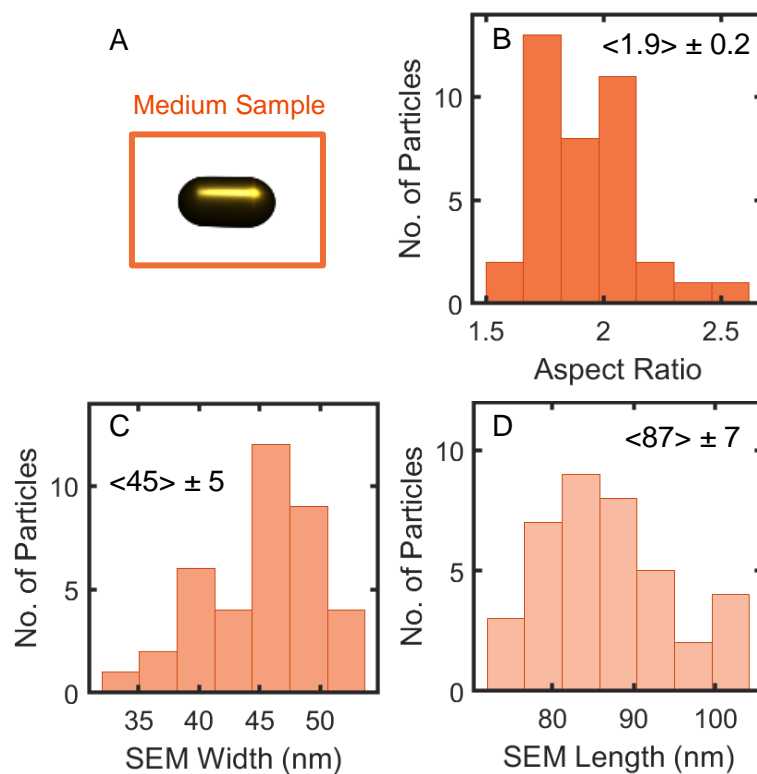


Figure 5-2 Characterization of medium AuNR sample (45 x 87 nm). (A) Representative scheme of medium AuNR sample (B) Histograms of aspect ratio, (C) width, and (D) length obtained from SEM images of all measured AuNRs in the medium samples.

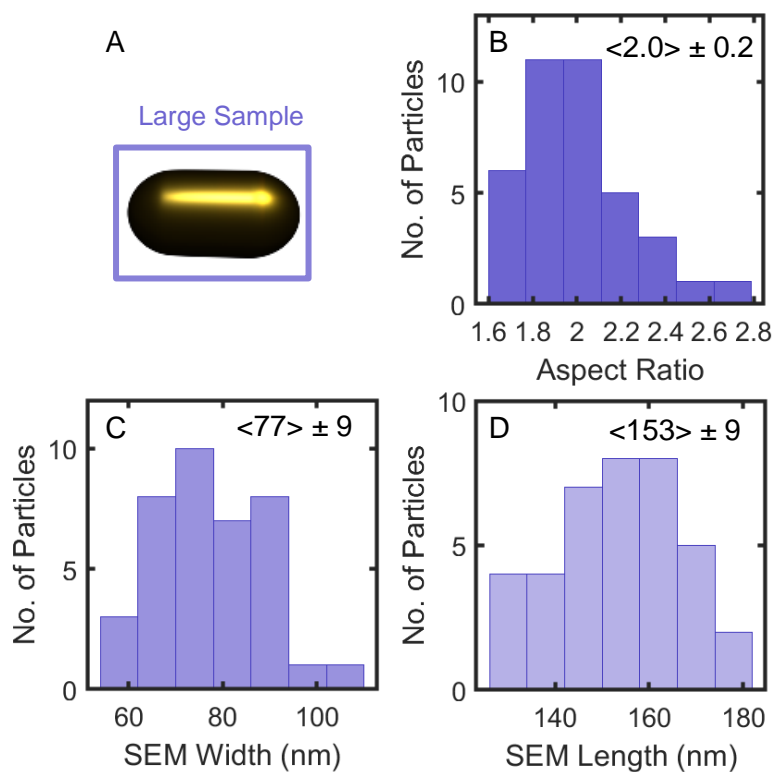


Figure 5-3 Characterization of large AuNR sample (77 x 153 nm). (A) Representative scheme of large AuNR sample (B) Histograms of aspect ratio, (C) width, and (D) length obtained from SEM images of all measured AuNRs in the large samples.

5.2. Quantum Yield Calculations and PL Spectral Scaling

The emission QYs of the AuNR samples were calculated according to a previously published method.³⁹ Here, QY (Φ) is defined as the ratio of emitted photons (N_{em}) to absorbed photons (N_{abs}).³⁹

$$\Phi = \frac{N_{em}}{N_{abs}}$$

Equation 5.1 – Definition of QY

First, the raw photon counts (N_{raw}) were determined by measuring photon counts obtained from APD images of single AuNRs in a 2 μm by 2 μm scanned area. N_{em} is then calculated by correcting the N_{raw} for the wavelength dependent efficiencies of the optics and filters used (Π) and photon detection efficiency of our detector (Det.Eff) using **Equation 5.2**.

$$N_{em} = \frac{N_{raw}}{\Pi \cdot \text{Det.Eff}}$$

Equation 5.2 – Number of emitted photons

A standard dye, rhodamine 6G, excited at 488 nm with a known absorption cross section and QY, was used to obtain a 1.6% Det.Eff for our setup. N_{abs} is determined using **Equation 5.3..**

$$N_{\text{abs}} = \frac{\sigma_{\text{abs}} I_{\text{exc}}}{h\nu_{\text{exc}}}$$

Equation 5.3 – Number of absorbed photons

The excitation intensity (I_{exc}) was found by measuring the power of the incident laser at the sample plane after the objective and dividing it by the beam waist. FDTD simulations were used to calculate the absorption cross section (σ_{abs}) of each individual AuNRs at the excitation wavelength based on the AuNR dimensions from SEM. Details regarding the FDTD simulations are discussed in the next section. The energy absorbed was converted into photons absorbed by dividing by $h\nu_{\text{exc}}$, the energy of the incident photons. The calculated QYs of individual AuNRs were then employed to scale the experimental emission spectra making it possible to directly compare all AuNRs acquired during different measurements. In the scaling procedure, integration of the emission spectra over the entire detected spectral region was first carried out. Spectral scaling was then performed in such a way that the integrated *scaled PL spectrum* is equal to the QY according to:

$$\Phi = \int \text{scaled PL spectrum}$$

Equation 5.4 – Scaling PL spectrum

5.3. FDTD Simulations

5.3.1. FDTD Simulations of AuNRs Absorption Cross Sections

The commercial software package Lumerical FDTD Solutions was used to determine the absorption cross sections of individual AuNRs for QY calculations as described in the previous section. The computational mesh size was set to 1 nm and the convergence criteria were set to default. Perfectly matched layers were used to avoid errors arising from reflections at the boundaries. A semi-infinite quartz substrate with a refractive index of 1.52 was included in the FDTD simulations.⁹⁵ Each AuNR's geometry was approximated as a capped hemispherical cylinder, covered with a 3.5 nm cetyltrimethylammonium bromide shell accounting for the ligand molecules; the refractive index of this dielectric layer was set to 1.44.⁹⁵ An example of the simulation configuration for an AuNR is shown in **Figure 5-4**. The bulk gold dielectric function measured by Johnson and Christy was employed to describe the AuNRs.⁹⁶ The dimensions each AuNR were set equal to the sizes measured by the correlated SEM images (FEI Quanta 400 ESEM FEG) and varied within the error of the SEM (i.e., ± 2 nm for small and medium AuNRs and ± 5 nm for large AuNRs) to achieve the best match between the simulated scattering spectrum maximum and the experimentally measured DFS maximum; the tolerable range for a match between simulation and experiment was when the maxima deviated by only ± 5 nm. After achieving such agreement, the absorption cross section of the AuNRs was determined at 488 nm and used in the QY calculations. **Figure 5-5** exemplifies a matched simulated scattering spectrum with experimental DFS spectrum. **Figure 5-5A** shows the SEM image of an AuNR with sizes

of 30.4 nm x 67.7 nm, the LSPR of this AuNR was analyzed to be at 618 nm by Lorentzian fitting. DFS spectrum is shown in **Figure 5-5C** with blue dashed lines. The best match for this AuNR was achieved with simulated sizes of 30 nm x 68 nm as shown in **Figure 5-5B** which possess an LSPR wavelength of 619 nm. **Figure 5-5C** overlays the simulated spectrum with the experimental DFS spectrum conveying an acceptable agreement between the simulation and experiment. After achieving the aforementioned agreement, the absorption cross section of the AuNRs at 488 nm was determined and used in QY calculations. **Figure 5-6** demonstrates the calculated absorption cross section of the correlated AuNR described in **Figure 5-5**.

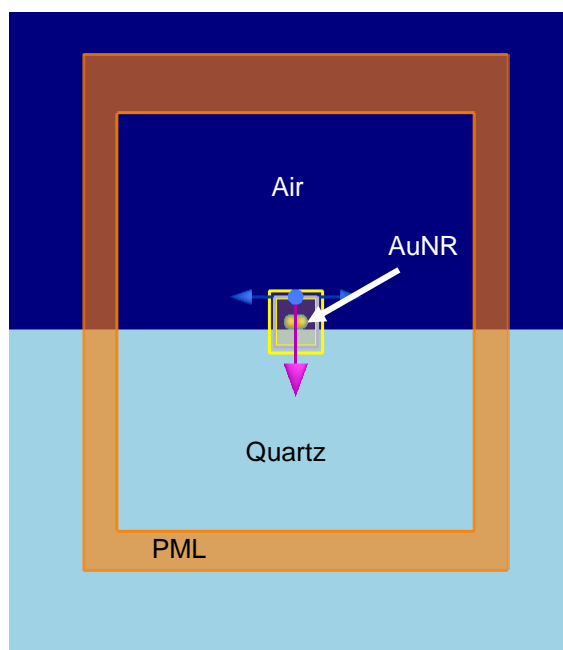


Figure 5-4 The configuration of AuNRs used in FDTD simulations (Lumerical). An AuNR approximated by a capped hemispherical cylinder and its 3.5 nm CTAB shell layer accounting for the ligand molecules is indicated by a white arrow that sits on the quartz substrate. The quartz substrate and air medium are also marked in the figure. The circularly polarized excitation source is depicted by the magenta arrow that excited the AuNR from top. The circularly polarized light is used to mimic the un-polarized illumination used in the experiment. The refractive index of quartz was set to 1.52 and that of CTAB shell was chosen to be 1.44⁹⁵. The dielectric constants of bulk gold was employed from experimental results of Johnson and Christy⁹⁶. The PML were used to surround the entire system.

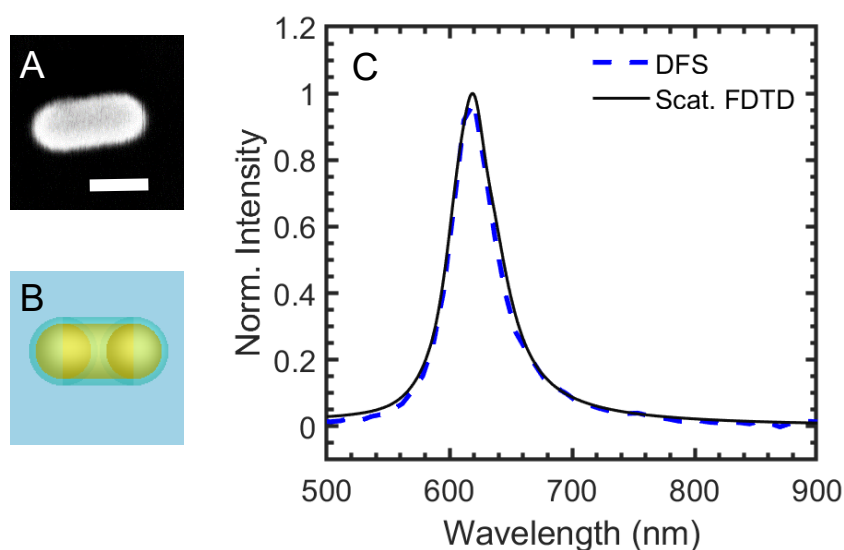


Figure 5-5 Correlated FDTD scattering cross section and experimental DFS spectrum agree well. (A) SEM image of the AuNR with the width of 30.4 nm and length of 67.7 nm. (B) Schematic representative of the simulated AuNR in FDTD. Best match with experimental scattering maximum was obtained by varying the width and length within 1 nm. Simulated AuNR with size of 30 nm x 68 nm provided the best match. (C) Correlated experimental DFS of AuNR presented in (A) with its FDTD simulated counterpart in (B). Maximum of experimental DFS and simulated scattering cross section were 618 nm and 619 nm, respectively.

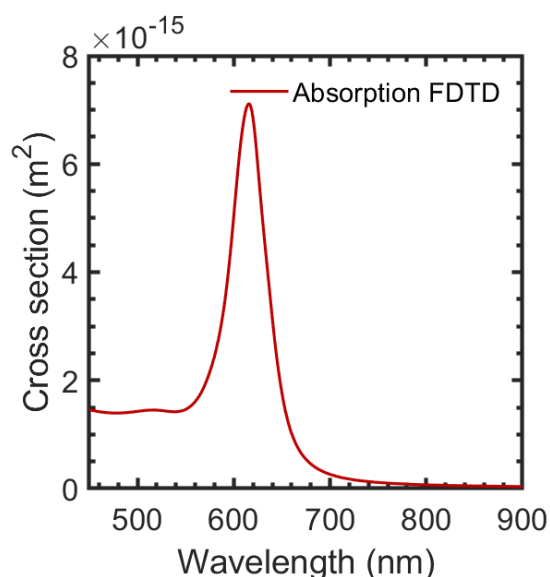


Figure 5-6 FDTD simulation of the absorption cross section of a single AuNR with sizes of 30 nm x 68 nm. The maximum of absorption cross section occurs around 615 nm suggesting a strong relationship to the LSPR of simulated AuNR.

The calculated absorption cross section at 488 nm for individual AuNRs is used in their QY calculations.

5.3.2. Near Field Electric Field Distribution Using FDTD Simulations

We also performed three dimensional FDTD simulations to find the near field electric field distribution of the AuNR at the AuNR-substrate interface. Calculating the electric field distribution was also followed after tuning the size to get the best match as described in the **section 5.3.1**. The schematic illustration of the three dimensional simulation configuration for the electric field simulations is depicted in **Figure 5-7**, which shows the simulation results will give the field distributions on the plane located at the interface of the AuNRs with substrate. The results of these simulations were used in the size dependency study of AuNRs in Chapter 4 where the details of the electric field confinement were obtained from electric field simulations.

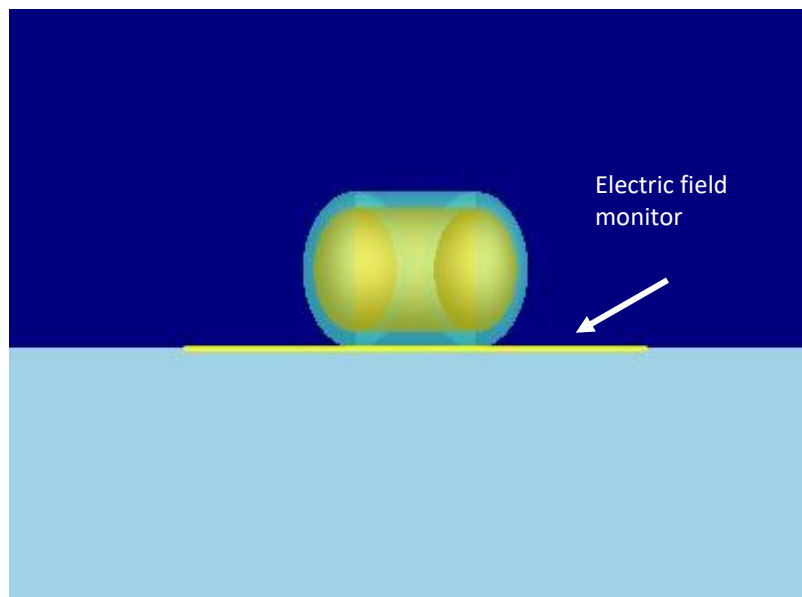


Figure 5-7 Schematic illustration of the used geometries to find the near field electric field distribution of the AuNRs at the particle-substrate interface plane.

5.3.3. Mode Volume Calculation

A procedure first introduced by Koenderink was employed to derive the mode volume:

90

$$V = \frac{\int (\text{Re}\epsilon + 2\omega\text{Im}\epsilon/\gamma)|E|^2 dr}{\max((\text{Re}\epsilon + 2\omega\text{Im}\epsilon/\gamma)|E|^2)}$$

Equation 5.5 – Mode volume calculation

In this procedure the energy density is defined as $(\text{Re}\epsilon + 2\omega\text{Im}\epsilon/\gamma) |E|^2$ for plasmonic nanostructures instead of $\epsilon|E|^2$ as the textbook definition of the mode volume.^{90, 97} The integral is calculated over all space, where ϵ is the dielectric constant taken from Johnson and Christy and γ is the Drude damping.⁹⁶ The resonance frequency is denoted by ω and $|E|^2$ is the square of the electric field, which was obtained through FDTD simulations as described above.

Chapter 6

Conclusions and Outlook

6.1. Overall Conclusions

In summary, we conducted a systematic study of the effect of size on the light emission of AuNRs. Our approach utilizes AuNRs with similar aspect ratios and hence similar resonances for the longitudinal mode, but different widths in order to have comparable contributions from interband damping.⁴⁰ Our single particle DFS and PL spectroscopy along with the correlated SEM images reveal the importance of AuNR geometry on the emission spectra and QY. We find a size dependence of inter- and intraband transitions contributing to the PL spectral lineshape and QY. Our results suggest that, in small AuNRs, intraband transitions are allowed due to the increased electric field confinement, breaking symmetry and momentum conservation rules. While interband transitions are the dominant contribution in the emission of large AuNRs and are only weakly dependent on size, a noticeable decrease in the emission of the large AuNRs is attributed to the decrease in the contribution from geometry-assisted intraband transitions. Finally, the role of the Purcell enhancement factor on the emission enhancement of AuNRs is demonstrated in agreement with Fermi's Golden rule for radiative recombination of excited charge carriers. We therefore conclude that the size dependence of the emission

from AuNRs observed and explained here is further evidence for an emission process involving hot carriers instead of electronic Raman scattering. Our results provide insight that can be used for characterizing hot carriers generated via plasmon excitation for potential applications in photocatalysis and photocurrent generation.

6.2. Outlook

Time-resolved emission spectroscopy using femtosecond luminescence upconversion techniques can be insightful to resolve the existing controversy on the origin of the emission.⁹⁸⁻⁹⁹ The measured lifetime for the luminescence will distinguish between the debated mechanisms (photoluminescence and electronic Raman scattering process) elucidating the origin of the light emission. While the expected lifetime for the photoluminescence mechanism is anticipated to be on the order of the electron-photon coupling timescale (~ 1 ps), the expected timescale for the inelastic electronic Raman Scattering process is only about the duration of the excitation pulse which is in the range of femtoseconds. Additionally, studies on establishing the precise relationship between the light emissions of plasmonic nanoparticles with the rate of hot carrier generation will be beneficial for optimizing hot carrier based devices.

References

1. Carattino, A.; Keizer, V. I. P.; Schaaf, M. J. M.; Orrit, M., Background Suppression in Imaging Gold Nanorods through Detection of Anti-Stokes Emission. *Biophys. J.* **2016**, *111* (11), 2492-2499.
2. Wang, H.; Huff, T. B.; Zweifel, D. A.; He, W.; Low, P. S.; Wei, A.; Cheng, J.-X., In vitro and in vivo two-photon luminescence imaging of single gold nanorods. *Proc. Natl. Acad. Sci. U. S. A.* **2005**, *102* (44), 15752-15756.
3. Imura, K.; Nagahara, T.; Okamoto, H., Near-Field Two-Photon-Induced Photoluminescence from Single Gold Nanorods and Imaging of Plasmon Modes. *The Journal of Physical Chemistry B* **2005**, *109* (27), 13214-13220.
4. Lu, G.; Hou, L.; Zhang, T.; Liu, J.; Shen, H.; Luo, C.; Gong, Q., Plasmonic Sensing via Photoluminescence of Individual Gold Nanorod. *J. Phys. Chem. C* **2012**, *116* (48), 25509-25516.
5. Tinguely, J.-C.; Sow, I.; Leiner, C.; Grand, J.; Hohenau, A.; Felidj, N.; Aubard, J.; Krenn, J. R., Gold Nanoparticles for Plasmonic Biosensing: The Role of Metal Crystallinity and Nanoscale Roughness. *BioNanoScience* **2011**, *1* (4), 128-135.
6. Kim, Y.; Johnson, R. C.; Hupp, J. T., Gold Nanoparticle-Based Sensing of “Spectroscopically Silent” Heavy Metal Ions. *Nano Lett.* **2001**, *1* (4), 165-167.
7. Zheng, Z.; Majima, T., Nanoplasmonic Photoluminescence Spectroscopy at Single-Particle Level: Sensing for Ethanol Oxidation. *Angewandte Chemie* **2016**, *128* (8), 2929-2933.
8. Carattino, A.; Caldarola, M.; Orrit, M., Gold Nanoparticles as Absolute Nanothermometers. *Nano Lett.* **2018**, *18* (2), 874-880.
9. Huang, J.; Wang, W.; Murphy, C. J.; Cahill, D. G., Resonant secondary light emission from plasmonic Au nanostructures at high electron temperatures created by pulsed-laser excitation. *Proceedings of the National Academy of Sciences* **2014**, *111* (3), 906.

10. Hugall, J. T.; Baumberg, J. J., Demonstrating Photoluminescence from Au is Electronic Inelastic Light Scattering of a Plasmonic Metal: The Origin of SERS Backgrounds. *Nano Lett.* **2015**, *15* (4), 2600-2604.
11. Hartland, G. V., Optical Studies of Dynamics in Noble Metal Nanostructures. *Chem. Rev.* **2011**, *111* (6), 3858-3887.
12. Shen, H.; Lu, G.; Zhang, T.; Liu, J.; Gu, Y.; Perriat, P.; Martini, M.; Tillement, O.; Gong, Q., Shape effect on a single-nanoparticle-based plasmonic nanosensor. *Nanotechnology* **2013**, *24* (28), 285502.
13. Cai, Y.-Y.; Liu, J. G.; Tauzin, L. J.; Huang, D.; Sung, E.; Zhang, H.; Joplin, A.; Chang, W.-S.; Nordlander, P.; Link, S., Photoluminescence of Gold Nanorods: Purcell Effect Enhanced Emission from Hot Carriers. *ACS Nano* **2018**, *12* (2), 976-985.
14. Fang, Y.; Chang, W.-S.; Willingham, B.; Swanglap, P.; Dominguez-Medina, S.; Link, S., Plasmon Emission Quantum Yield of Single Gold Nanorods as a Function of Aspect Ratio. *ACS Nano* **2012**, *6* (8), 7177-7184.
15. Tcherniak, A.; Dominguez-Medina, S.; Chang, W.-S.; Swanglap, P.; Slaughter, L. S.; Landes, C. F.; Link, S., One-Photon Plasmon Luminescence and Its Application to Correlation Spectroscopy as a Probe for Rotational and Translational Dynamics of Gold Nanorods. *J. Phys. Chem. C* **2011**, *115* (32), 15938-15949.
16. Yin, T.; Jiang, L.; Shen, Z., Recent progress on photoluminescence from plasmonic nanostructures: Phenomenon, mechanism, and application. *Chinese Physics B* **2018**, *27* (9), 097803.
17. Zhang, W.; Wen, T.; Cheng, Y.; Zhao, J.; Gong, Q.; Lü, G., Intrinsic luminescence from metal nanostructures and its applications. *Chinese Physics B* **2018**, *27* (9), 097302.
18. Imura, K.; Okamoto, H., Properties of Photoluminescence from Single Gold Nanorods Induced by Near-Field Two-Photon Excitation. *Journal of Physical Chemistry C* **2009**, *113* (27), 11756-11759.
19. Khatua, S.; Paulo, P. M. R.; Yuan, H.; Gupta, A.; Zijlstra, P.; Orrit, M., Resonant Plasmonic Enhancement of Single-Molecule Fluorescence by Individual Gold Nanorods. *ACS Nano* **2014**, *8* (5), 4440-4449.

20. Eustis, S.; El-Sayed, M., Aspect Ratio Dependence of the Enhanced Fluorescence Intensity of Gold Nanorods: Experimental and Simulation Study. *J. Phys. Chem. B* **2005**, *109* (34), 16350-16356.
21. Yorulmaz, M.; Khatua, S.; Zijlstra, P.; Gaiduk, A.; Orrit, M., Luminescence Quantum Yield of Single Gold Nanorods. *Nano Letters* **2012**, *12* (8), 4385-4391.
22. Mooradian, A., Photoluminescence of Metals. *Appl. Phys. Lett.* **1969**, *22* (5), 185-187.
23. Boyd, G. T.; Yu, Z. H.; Shen, Y. R., Photoinduced luminescence from the noble metals and its enhancement on roughened surfaces. *Phys. Rev. B* **1986**, *33* (12), 7923-7936.
24. Beversluis, M. R.; Bouhelier, A.; Novotny, L., Continuum generation from single gold nanostructures through near-field mediated intraband transitions. *Phys. Rev. B* **2003**, *68* (11), 115433.
25. Haug, T.; Klemm, P.; Bange, S.; Lupton, J. M., Hot-Electron Intraband Luminescence from Single Hot Spots in Noble-Metal Nanoparticle Films. *Physical Review Letters* **2015**, *115* (6), 067403.
26. Wilcoxon, J. P.; Martin, J. E.; Parsapour, F.; Wiedenman, B.; Kelley, D. F., Photoluminescence from nanosize gold clusters. *The Journal of Chemical Physics* **1998**, *108* (21), 9137-9143.
27. Mohamed, M. B.; Volkov, V.; Link, S.; El-Sayed, M. A., The 'lightning' gold nanorods: fluorescence enhancement of over a million compared to the gold metal. *Chem. Phys. Lett.* **2000**, *317* (6), 517-523.
28. Dulkeith, E.; Niedereichholz, T.; Klar, T. A.; Feldmann, J.; von Plessen, G.; Gittins, D. I.; Mayya, K. S.; Caruso, F., Plasmon emission in photoexcited gold nanoparticles. *Physical Review B* **2004**, *70* (20), 205424.
29. Gaiduk, A.; Yorulmaz, M.; Orrit, M., Correlated Absorption and Photoluminescence of Single Gold Nanoparticles. *ChemPhysChem* **2011**, *12* (8), 1536-1541.

30. Imura, K.; Okamoto, H., Properties of Photoluminescence from Single Gold Nanorods Induced by Near-Field Two-Photon Excitation. *The Journal of Physical Chemistry C* **2009**, *113* (27), 11756-11759.
31. Lumdee, C.; Yun, B.; Kik, P. G., Gap-Plasmon Enhanced Gold Nanoparticle Photoluminescence. *ACS Photonics* **2014**, *1* (11), 1224-1230.
32. Apell, P.; Monreal, R.; Lundqvist, S., Photoluminescence of noble metals. *Phys. Scr.* **1988**, *38* (2), 174-179.
33. Zheng, J.; Zhou, C.; Yu, M.; Liu, J., Different sized luminescent gold nanoparticles. *Nanoscale* **2012**, *4* (14), 4073-4083.
34. Sönnichsen, C.; Franzl, T.; Wilk, T.; von Plessen, G.; Feldmann, J.; Wilson, O.; Mulvaney, P., Drastic Reduction of Plasmon Damping in Gold Nanorods. *Appl. Phys. Lett.* **2002**, *88* (7), 077402.
35. Mertens, J.; Kleemann, M.-E.; Chikkaraddy, R.; Narang, P.; Baumberg, J. J., How Light Is Emitted by Plasmonic Metals. *Nano Lett.* **2017**, *17* (4), 2568-2574.
36. Dey, S.; Banik, M.; Hulkko, E.; Rodriguez, K.; Apkarian, V. A.; Galperin, M.; Nitzan, A., Observation and analysis of Fano-like lineshapes in the Raman spectra of molecules adsorbed at metal interfaces. *Phys. Rev. B* **2016**, *93* (3), 035411.
37. Hu, H.; Duan, H.; Yang, J. K. W.; Shen, Z. X., Plasmon-Modulated Photoluminescence of Individual Gold Nanostructures. *ACS Nano* **2012**, *6* (11), 10147-10155.
38. Yorulmaz, M.; Khatua, S.; Zijlstra, P.; Gaiduk, A.; Orrit, M., Luminescence Quantum Yield of Single Gold Nanorods. *Nano Lett.* **2012**, *12* (8), 4385-4391.
39. Huang, D.; Byers, C. P.; Wang, L.-Y.; Hoggard, A.; Hoener, B.; Dominguez-Medina, S.; Chen, S.; Chang, W.-S.; Landes, C. F.; Link, S., Photoluminescence of a Plasmonic Molecule. *ACS Nano* **2015**, *9* (7), 7072-7079.
40. Tauzin, L. J.; Cai, Y.-Y.; Smith, K. W.; Hosseini Jebeli, S. A.; Bhattacharjee, U.; Chang, W.-S.; Link, S., Exploring the Relationship between Plasmon Damping and Luminescence in Lithographically Prepared Gold Nanorods. *ACS Photonics* **2018**, *5* (9), 3541-3549.

41. Yang, J.; Sun, Q.; Ueno, K.; Shi, X.; Oshikiri, T.; Misawa, H.; Gong, Q., Manipulation of the dephasing time by strong coupling between localized and propagating surface plasmon modes. *Nature Communications* **2018**, *9* (1), 4858.
42. Grubisic, A.; Schweikhard, V.; Baker, T. A.; Nesbitt, D. J., Coherent Multiphoton Photoelectron Emission from Single Au Nanorods: The Critical Role of Plasmonic Electric Near-Field Enhancement. *ACS Nano* **2013**, *7* (1), 87-99.
43. Zhang, W.; Cheng, Y.; Zhao, J.; Wen, T.; Hu, A.; Gong, Q.; Lu, G., Photoluminescence Quantum Yield from Gold Nanorods: Dependence on Excitation Polarization. *J. Phys. Chem. C* **2019**, *123* (14), 9358-9363.
44. Andersen, S. K. H.; Pors, A.; Bozhevolnyi, S. I., Gold Photoluminescence Wavelength and Polarization Engineering. *ACS Photonics* **2015**, *2* (3), 432-438.
45. Schmidt, T.; Lischka, K.; Zulehner, W., Excitation-power dependence of the near-band-edge photoluminescence of semiconductors. *Phys. Rev. B* **1992**, *45* (16), 8989-8994.
46. Fröhlich, T.; Schönenberger, C.; Calame, M., Additional peak appearing in the one-photon luminescence of single gold nanorods. *Opt. Lett.* **2016**, *41* (7), 1325-1328.
47. Xie, X.; Cahill, D. G., Thermometry of plasmonic nanostructures by anti-Stokes electronic Raman scattering. *Appl. Phys. Lett.* **2016**, *109* (18), 183104.
48. Jones, S.; Andrén, D.; Karpinski, P.; Käll, M., Photothermal Heating of Plasmonic Nanoantennas: Influence on Trapped Particle Dynamics and Colloid Distribution. *ACS Photonics* **2018**, *5* (7), 2878-2887.
49. Hartland, G. V.; Besteiro, L. V.; Johns, P.; Govorov, A. O., What's so Hot about Electrons in Metal Nanoparticles? *ACS Energy Lett.* **2017**, *2* (7), 1641-1653.
50. Brongersma, M. L.; Halas, N. J.; Nordlander, P., Plasmon-induced hot carrier science and technology. *Nat. Nanotechnol.* **2015**, *10* (1), 25-34.
51. Zheng, B. Y.; Zhao, H.; Manjavacas, A.; McClain, M.; Nordlander, P.; Halas, N. J., Distinguishing between plasmon-induced and photoexcited carriers in a device geometry. *Nat. Commun.* **2015**, *6*.

52. Mubeen, S.; Lee, J.; Singh, N.; Krämer, S.; Stucky, G. D.; Moskovits, M., An autonomous photosynthetic device in which all charge carriers derive from surface plasmons. *Nat. Nanotechnol.* **2013**, *8*, 247-251.
53. Clavero, C., Plasmon-induced hot-electron generation at nanoparticle/metal-oxide interfaces for photovoltaic and photocatalytic devices. *Nat. Photonics* **2014**, *8*, 95-103.
54. Manjavacas, A.; Liu, J. G.; Kulkarni, V.; Nordlander, P., Plasmon-Induced Hot Carriers in Metallic Nanoparticles. *ACS Nano* **2014**, *8* (8), 7630-7638.
55. Narang, P.; Sundararaman, R.; Jermyn, A. S.; Goddard, W. A.; Atwater, H. A., Cubic Nonlinearity Driven Up-Conversion in High-Field Plasmonic Hot Carrier Systems. *J. Phys. Chem. C* **2016**, *120* (37), 21056-21062.
56. Tagliabue, G.; Jermyn, A. S.; Sundararaman, R.; Welch, A. J.; DuChene, J. S.; Pala, R.; Davoyan, A. R.; Narang, P.; Atwater, H. A., Quantifying the role of surface plasmon excitation and hot carrier transport in plasmonic devices. *Nat. Commun.* **2018**, *9* (1), 3394.
57. Sundararaman, R.; Narang, P.; Jermyn, A. S.; Goddard, W. A.; Atwater, H. A., Theoretical predictions for hot-carrier generation from surface plasmon decay. *Nat. Commun.* **2014**, *5*.
58. Christopher, P.; Xin, H.; Marimuthu, A.; Linic, S., Singular characteristics and unique chemical bond activation mechanisms of photocatalytic reactions on plasmonic nanostructures. *Nat. Mater.* **2012**, *11*, 1044.
59. Mukherjee, S.; Zhou, L.; Goodman, A. M.; Large, N.; Ayala-Orozco, C.; Zhang, Y.; Nordlander, P.; Halas, N. J., Hot-Electron-Induced Dissociation of H₂ on Gold Nanoparticles Supported on SiO₂. *J. Am. Chem. Soc.* **2014**, *136* (1), 64-67.
60. Khurgin, J. B., How to deal with the loss in plasmonics and metamaterials. *Nat. Nanotechnol.* **2015**, *10*, 2.
61. Jin, R.; Charles Cao, Y.; Hao, E.; Métraux, G. S.; Schatz, G. C.; Mirkin, C. A., Controlling anisotropic nanoparticle growth through plasmon excitation. *Nature* **2003**, *425* (6957), 487-490.

62. Wu, X.; Thrall, E. S.; Liu, H.; Steigerwald, M.; Brus, L., Plasmon Induced Photovoltage and Charge Separation in Citrate-Stabilized Gold Nanoparticles. *J. Phys. Chem. C* **2010**, *114* (30), 12896-12899.
63. Thrall, E. S.; Preska Steinberg, A.; Wu, X.; Brus, L. E., The Role of Photon Energy and Semiconductor Substrate in the Plasmon-Mediated Photooxidation of Citrate by Silver Nanoparticles. *J. Phys. Chem. C* **2013**, *117* (49), 26238-26247.
64. Wu, K.; Rodríguez-Córdoba, W. E.; Yang, Y.; Lian, T., Plasmon-Induced Hot Electron Transfer from the Au Tip to CdS Rod in CdS-Au Nanoheterostructures. *Nano Lett.* **2013**, *13* (11), 5255-5263.
65. Lin, K. Q.; Yi, J.; Hu, S.; Sun, J. J.; Zheng, J. T.; Wang, X.; Ren, B., Intraband Hot-Electron Photoluminescence from Single Silver Nanorods. *Acs Photonics* **2016**, *3* (7), 1248-1255.
66. Lin, K.-Q.; Yi, J.; Hu, S.; Sun, J.-J.; Zheng, J.-T.; Wang, X.; Ren, B., Intraband Hot-Electron Photoluminescence from Single Silver Nanorods. *ACS Photonics* **2016**, *3* (7), 1248-1255.
67. Foerster, B.; Joplin, A.; Kaefer, K.; Celiksoy, S.; Link, S.; Sönnichsen, C., Chemical Interface Damping Depends on Electrons Reaching the Surface. *ACS Nano* **2017**, *11* (3), 2886-2893.
68. Lin, K.-Q.; Yi, J.; Hu, S.; Liu, B.-J.; Liu, J.-Y.; Wang, X.; Ren, B., Size Effect on SERS of Gold Nanorods Demonstrated via Single Nanoparticle Spectroscopy. *J. Phys. Chem. C* **2016**, *120* (37), 20806-20813.
69. Perner, M.; Bost, P.; Lemmer, U.; von Plessen, G.; Feldmann, J.; Becker, U.; Mennig, M.; Schmitt, M.; Schmidt, H., Optically Induced Damping of the Surface Plasmon Resonance in Gold Colloids. *Appl. Phys. Lett.* **1997**, *78* (11), 2192-2195.
70. Gans, R., Über die Form ultramikroskopischer Silberteilchen. *Ann. Phys. (Berlin, Ger.)* **1915**, *352* (10), 270-284.
71. Slaughter, L. S.; Chang, W.-S.; Swanglap, P.; Tcherniak, A.; Khanal, B. P.; Zubarev, E. R.; Link, S., Single-Particle Spectroscopy of Gold Nanorods beyond the Quasi-Static Limit: Varying the Width at Constant Aspect Ratio. *J. Phys. Chem. C* **2010**, *114* (11), 4934-4938.

72. Shahbazyan, T. V., Theory of Plasmon-Enhanced Metal Photoluminescence. *Nano Lett.* **2013**, *13* (1), 194-198.
73. Bouhelier, A.; Bachelot, R.; Lerondel, G.; Kostcheev, S.; Royer, P.; Wiederrecht, G. P., Surface Plasmon Characteristics of Tunable Photoluminescence in Single Gold Nanorods. *Appl. Phys. Lett.* **2005**, *95* (26), 267405.
74. Cai, Y.-Y.; Sung, E.; Zhang, R.; Tauzin, L. J.; Liu, J. G.; Ostovar, B.; Zhang, Y.; Chang, W.-S.; Nordlander, P.; Link, S., Anti-Stokes Emission from Hot Carriers in Gold Nanorods. *Nano Lett.* **2019**, *19* (2), 1067-1073.
75. Oldenburg, S. J.; Hale, G. D.; Jackson, J. B.; Halas, N. J., Light scattering from dipole and quadrupole nanoshell antennas. *Appl. Phys. Lett.* **1999**, *75* (8), 1063-1065.
76. Joplin, A.; Chang, W.-S.; Link, S., Imaging and Spectroscopy of Single Metal Nanostructure Absorption. *Langmuir* **2018**, *34* (13), 3775-3786.
77. Bohren, C. F.; Huffman, D. R., *Absorption and Scattering of Light by Small Particles*. Wiley, New York: 1983.
78. Kreibig, U.; Vollmer, M., *Optical Properties of Metal Clusters*. Springer: Berlin: 1995.
79. He, Y.; Xia, K.; Lu, G.; Shen, H.; Cheng, Y.; Liu, Y.-c.; Shi, K.; Xiao, Y.-F.; Gong, Q., Surface enhanced anti-Stokes one-photon luminescence from single gold nanorods. *Nanoscale* **2015**, *7* (2), 577-582.
80. Lermé, J.; Baida, H.; Bonnet, C.; Broyer, M.; Cottancin, E.; Crut, A.; Maioli, P.; Del Fatti, N.; Vallée, F.; Pellarin, M., Size Dependence of the Surface Plasmon Resonance Damping in Metal Nanospheres. *J. Phys. Chem. Lett.* **2010**, *1* (19), 2922-2928.
81. Hohenester, U.; Trügler, A., MNPBEM – A Matlab toolbox for the simulation of plasmonic nanoparticles. *Comput. Phys. Commun.* **2012**, *183* (2), 370-381.
82. Shang, L.; Dong, S., Design of Fluorescent Assays for Cyanide and Hydrogen Peroxide Based on the Inner Filter Effect of Metal Nanoparticles. *Anal. Chem.* **2009**, *81* (4), 1465-1470.

83. Ullrich, B.; Schroeder, R.; Graupner, W.; Sakai, H., The influence of self-absorption on the photoluminescence of thin film CdS demonstrated by two-photon absorption. *Opt. Express* **2001**, *9* (3), 116-120.
84. Heilpern, T.; Manjare, M.; Govorov, A. O.; Wiederrecht, G. P.; Gray, S. K.; Harutyunyan, H., Determination of hot carrier energy distributions from inversion of ultrafast pump-probe reflectivity measurements. *Nat. Commun.* **2018**, *9* (1), 1853.
85. Bigioni, T. P.; Whetten, R. L.; Dag, Ö., Near-Infrared Luminescence from Small Gold Nanocrystals. *J. Phys. Chem. B* **2000**, *104* (30), 6983-6986.
86. Zurita-Sánchez, J. R.; Novotny, L., Multipolar interband absorption in a semiconductor quantum dot. I. Electric quadrupole enhancement. *J. Opt. Soc. Am. B* **2002**, *19* (6), 1355-1362.
87. Khurgin, J.; Tsai, W.-Y.; Tsai, D. P.; Sun, G., Landau Damping and Limit to Field Confinement and Enhancement in Plasmonic Dimers. *ACS Photonics* **2017**, *4* (11), 2871-2880.
88. Zhang, H.; Govorov, A. O., Optical Generation of Hot Plasmonic Carriers in Metal Nanocrystals: The Effects of Shape and Field Enhancement. *J. Phys. Chem. C* **2014**, *118* (14), 7606-7614.
89. Novotny, L.; Hecht, B., *Principles of Nano-Optics* Cambridge University: 2006.
90. Koenderink, A. F., On the use of Purcell factors for plasmon antennas. *Opt. Lett.* **2010**, *35* (24), 4208-4210.
91. Bosman, M.; Zhang, L.; Duan, H.; Tan, S. F.; Nijhuis, C. A.; Qiu, C. W.; Yang, J. K. W., Encapsulated Annealing: Enhancing the Plasmon Quality Factor in Lithographically-Defined Nanostructures. *Sci. Rep.* **2014**, *4*, 5537.
92. Sauvan, C.; Hugonin, J. P.; Maksymov, I. S.; Lalanne, P., Theory of the Spontaneous Optical Emission of Nanosize Photonic and Plasmon Resonators. *Appl. Phys. Lett.* **2013**, *110* (23), 237401.
93. Ye, X.; Zheng, C.; Chen, J.; Gao, Y.; Murray, C. B., Using Binary Surfactant Mixtures To Simultaneously Improve the Dimensional Tunability and Monodispersity in the Seeded Growth of Gold Nanorods. *Nano Lett.* **2013**, *13* (2), 765-771.

94. Ming, T.; Feng, W.; Tang, Q.; Wang, F.; Sun, L.; Wang, J.; Yan, C., Growth of Tetrahedral Gold Nanocrystals with High-Index Facets. *Journal of the American Chemical Society* **2009**, *131* (45), 16350-16351.
95. Martinsson, E.; Shahjamali, M. M.; Large, N.; Zraee, N.; Zhou, Y.; Schatz, G. C.; Mirkin, C. A.; Aili, D., Influence of Surfactant Bilayers on the Refractive Index Sensitivity and Catalytic Properties of Anisotropic Gold Nanoparticles. *Small* **2016**, *12* (3), 330-342.
96. Johnson, P. B.; Christy, R. W., Optical Constants of the Noble Metals. *Phys. Rev. B* **1972**, *6* (12), 4370-4379.
97. Ruppin, R., Electromagnetic energy density in a dispersive and absorptive material. *Physics Letters A* **2002**, *299* (2), 309-312.
98. Hwang, Y.-N.; Jeong, D. H.; Shin, H. J.; Kim, D.; Jeoung, S. C.; Han, S. H.; Lee, J.-S.; Cho, G., Femtosecond Emission Studies on Gold Nanoparticles. *The Journal of Physical Chemistry B* **2002**, *106* (31), 7581-7584.
99. Varnavski, O. P.; Mohamed, M. B.; El-Sayed, M. A.; Goodson, T., Relative Enhancement of Ultrafast Emission in Gold Nanorods. *The Journal of Physical Chemistry B* **2003**, *107* (14), 3101-3104.